# Using $^{226}$Ra and $^{228}$Ra isotopes to distinguish water mass distribution in the Canadian Arctic Archipelago

Chantal Mears[1,2], Helmuth Thomas[2,1*], Paul B. Henderson[3], Matthew A. Charette[3], Hugh MacIntyre[1], Frank Dehairs[4], Christophe Monnin[5], and Alfonso Mucci[6]

[1]: Dalhousie University, Department of Oceanography, Halifax, NS, Canada

[2]: Helmholtz-Centre-Geesthacht, Institute for Coastal Research, Geesthacht, Germany.

[3]: Woods Hole Oceanographic Institution, Department of Marine Chemistry and Geochemistry, Woods Hole, MA, USA.

[4]: Earth System Sciences and Analytical and Environmental Chemistry, Vrije Universiteit Brussel, Brussels, Belgium.

[5]: CNRS -Université Paul Sabatier-IRD-OMP, Geosciences Environnement Toulouse (GET), 14 Avenue Edouard Belin, 31400 Toulouse FRANCE

[6]: GEOTOP and Department of Earth and Planetary Sciences, McGill University, Montréal, QC, Canada

[*]: corresponding author, email: helmuth.thomas@hzg.de

**Abstract:**

As a shelf dominated basin, the Arctic Ocean and its biogeochemistry are heavily influenced by continental and riverine sources. Radium isotopes ($^{226}$Ra, $^{228}$Ra, $^{224}$Ra, $^{223}$Ra), are transferred from the sediments to seawater, making them ideal tracers of sediment-water exchange processes and ocean mixing. As the two long-lived isotopes of the Radium Quartet, $^{226}$Ra and $^{228}$Ra ($^{226}$Ra, $t_{1/2}$=1600y and $^{228}$Ra, $t_{1/2}$=5.8y) can provide insight into the water mass compositions, distribution patterns, as well as mixing processes and the associated timescales throughout the Canadian Arctic Archipelago (CAA). The wide range of $^{226}$Ra and $^{228}$Ra activities, as well as of the $^{228}$Ra/$^{226}$Ra ratios, measured in water samples collected during the 2015 GEOTRACES cruise, complemented by additional chemical tracers (dissolved inorganic carbon (DIC), total alkalinity (AT), barium (Ba), and the stable oxygen isotope composition of water ($\delta^{18}$O)), highlight the dominant biogeochemical, hydrographic and bathymetric features of the CAA. Bathymetric features, such as the continental shelf and shallow coastal sills, are critical in modulating circulation patterns within the CAA, including the bulk flow of Pacific waters and the inhibited eastward flow of denser Atlantic waters through the CAA. Using a Principal Component Analysis, we unravel the dominant mechanisms and apparent water mass end-members that shape the tracer distributions. We identify two distinct water masses located above and below the upper halocline layer throughout the CAA, as well as distinctly differentiate surface waters in the eastern and western CAA. Furthermore, we highlight water exchange across 80°W, inferring a draw of Atlantic water, originating from Baffin Bay, into the CAA. This underscores the presence of an Atlantic water U-turn located at Barrow Strait, where the same water mass is seen along the northernmost edge at 80°W as well as along the south-eastern most confines of Lancaster Sound. Overall, this study provides a stepping stone for future research initiatives within the Canadian Arctic Archipelago, revealing how quantifying disparities in the distributions of radioactive tracers can provide valuable information on

water mass distributions, flow patterns and mixing, within vulnerable areas such as the CAA.

## I: Introduction

### I.I. General Background

Over the past 30 years, major research initiatives have been undertaken within the Arctic, highlighting this region's global importance and vulnerability to climate change (Prinsenberg and Bennett, 1987; Shadwick et al., 2013). One of the primary causes of this vulnerability is a modification of the regional hydrographic regime, characterized by cool, $CO_2$-charged (less alkaline) Pacific waters, that enter the Arctic Ocean via the Bering Strait, flowing along the southern parts of the Canadian Arctic Archipelago (CAA) and being dispersed into Baffin Bay. Previous studies have shown that these eastward flowing waters contribute significantly to carbon sequestration as well as instigate deep-water formation in the North Atlantic (e.g., Aagaard and Carmack, 1989; Burt et al., 2016a; Curry et al., 2011; Hamilton and Wu, 2013; Holland et al., 2001; Ingram and Prinsenberg, 1998; Rahmstorf, 2002; Shadwick et al., 2011a).

Although the various water masses delivered to Baffin Bay play a role in establishing and maintaining the global thermohaline circulation, little is known about the distribution, composition, and modes of delivery of water through the Canadian Archipelago. This study contributes to the knowledge base of circulation patterns in the CAA by using the radioactive radium isotopes $^{228}Ra$ and $^{226}Ra$ as well as dissolved inorganic carbon (DIC), total alkalinity (AT), barium (Ba), and the stable oxygen isotope composition of water ($\delta^{18}O$) as tracers of water mass distribution, mixing, and composition throughout the region. Moreover, we hope that this study will provide a foundation for further investigations of how changes in environmental conditions within this vulnerable area will affect the distribution of these tracers, as well as biogeochemical cycles and circulation in the CAA.

I.II. Oceanographic Setting

Approximately 30-50% of the Arctic Ocean surface area (totaling to $9.5x10^6 km^2$) is dominated by polar continental shelves (Coachman and Aagaard, 1974; Jakobsson, 2002; Rutgers van der Loeff et al., 1995; Shadwick et al., 2011b; Walsh, 1991; Xing et al., 2003). The CAA, a region of branching channels and straits that extends from approximately 120°W to 80°W is located in this shelf-dominated region (Fig. 1). Spanning only 65km across at its widest, this narrow, polar network provides a critical connection between the Pacific and Atlantic Oceans and facilitates the export of approximately one third of the Arctic Ocean's outflowing water (Coachman and Aagaard, 1974; Hamilton et al., 2013; Hamilton and Wu, 2013).

Previous research has recognized the partitioning of the water column in the CAA into three salinity-defined water masses, the deepest and most saline being the Atlantic Layer (ATL, $S_p$ >33.1), followed by the Pacific Upper Halocline Layer (UHL; $31 < S_P < 33.1$), and finally the least saline and uppermost being the Polar Mixed Layer (PML; $S_P$ <31) (e.g., Aagaard et al., 1981; Aagaard and Carmack, 1994; Bauch et al., 1995; Mathis et al., 2005; Shadwick et al., 2011a). All three water masses have been identified at both the eastern and western boundaries of the CAA whereas only the upper two layers (PML and UHL) are found throughout. The presence of a 200 m shoal at Barrow Strait (Fig. 1), that bridges the western and eastern regions, prevents the Deep ATL water mass from flowing eastward through the CAA (Jones, 2003; Macdonald et al., 1987; Newton and Coachman, 1974). As a result, the bulk eastward transport is composed of the cool, $CO_2$-charged (less alkaline) Pacific and fresh surface waters that flow from the Canada Basin to Baffin Bay through the CAA (Hamilton and Wu, 2013; Prinsenberg et al., 2009; Wang et al., 2012; Xing et al., 2003).

In addition to the bulk eastward transport through the CAA, the northern regions of the CAA host an occasional westward flowing counter-current during late summer (Peterson et al., 2012; Prinsenberg & Bennett, 1987; Prinsenberg et al., 2009; Rudels, 1985). This suggests that there may be the intrusion of

Atlantic waters originating from Baffin Bay, moving into the CAA along the northern edge from the east, and possibly creating a “U-turn” as the westward current reroutes back into Baffin Bay along the southern edge. The importance of this “U-turn” will be discussed later in the results section.

I.III. Some considerations about the two long-lived Radium Isotopes

$^{226}$Ra and $^{228}$Ra are the two longer-lived isotopes of the Radium Quartet ($^{226}$Ra, $t_{1/2}$=1600 y and $^{228}$Ra, $t_{1/2}$=5.8 y) and are often present at readily detectable activities that are largely unperturbed by biological activity in seawater. $^{226}$Ra and $^{228}$Ra are thus often considered as conservative radioactive tracers (Charette et al., 2015a, 2016; International Atomic Energy Agency (IAEA), 2010; Moore et al., 1980). Both long-lived Ra isotopes are formed from the decay of different Thorium (Th) isotopes ($^{226}$Ra is the daughter of $^{230}$Th, whereas $^{228}$Ra is the daughter of $^{232}$Th) in terrestrial soils and marine sediments. Subsequently, they are distributed to the ocean through riverine inputs, porewater advection, and diffusion across the sediment-water interface (Charette et al., 2015a). Since $^{228}$Ra is more rapidly regenerated within sediments and its half-life is relatively short in comparison to $^{226}$Ra, its activity in coastal and continental shelf regions decreases rapidly away from the source towards the open ocean. Thus, $^{228}$Ra tracks the sediment-ocean or shelf-ocean transition (van Beek et al., 2007; Burt et al., 2016b; Kadko and Muench, 2005; Kawakami and Kusakabe, 2008; Moore et al., 1980, 2008; Rutgers van der Loeff et al., 1995). For the purpose of this study, we assume that $^{228}$Ra has no pelagic source. As $^{226}$Ra is released from the sediment and disperses into the water column through advective and diffusive mixing (Charette et al., 2015a; International Atomic Energy Agency (IAEA), 2010; Rutgers van der Loeff and Moore, 1999), its longer half-life allows it to be distributed over great distances, often decaying within the oceanic water column (Charette et al., 2015a; International Atomic Energy Agency (IAEA), 1988). A slight enrichment in Pacific Ocean deep waters, relative to deep waters of the Atlantic Ocean is primarily attributed to $^{226}$Ra uptake in the co-precipitation of barite ($BaSO_4$) or its

uptake by biological silicate or calcium tests (van Beek et al., 2007; Charette et al., 2015b; Moore and Dymond, 1991). With this exception, $^{226}$Ra displays a “nearly” conservative distribution in the oceans, thus facilitating its use as a long-term pelagic-based tracer of water masses and of shelf inputs (Broecker et al., 1967; Charette et al., 2015a; Chung, 1980). These characteristics allow the two long-lived Ra isotopes to be used as radioactive geochemical tracers to distinguish water mass sources and their distribution patterns within the CAA.

## II. Methods

### II.I. Sample Collection

During the summer of 2015 Canadian GEOTRACES cruise, 64 water samples were collected throughout the Canadian Arctic Archipelago aboard the icebreaker CCGS Amundsen at 17 different stations as a subset of the overall biogeochemical sampling (Fig. 1). Samples for dissolved inorganic carbon (DIC), total alkalinity (AT), barium (Ba), the stable oxygen isotope composition of water ($\delta^{18}O$), and Ra isotopes were collected at various depths from the surface to 1000m on the up-cast of a rosette system equipped with (24) 12-L Niskin bottles. Surface samples (2-12m) for Ra were collected using an onboard pump collecting ship-side. In addition, temperature and salinity ($S_P$) measurements were recorded on the downcast by a Sea-Bird SBE 9 (Seasave V 7.23.2) CTD. The CTD salinity-probe measurements were calibrated post-cruise using a Guidline salinometer in the home laboratory against discrete samples taken directly from the Niskin bottles into 250 mL screw-cap HDPE bottles. DIC and AT samples were collected directly from the Niskin bottles into 250mL or 500mL borosilicate glass bottles to which 100µL of a saturated $HgCl_2$ solution was added before being sealed with ground-glass stoppers, Apiezon® Type-M grease and elastic closures (Burt et al., 2016a). The bottles were then stored in the dark at room temperature or 4°C until they could be processed on board. A VINDTA 3C (Versatile Instrument for the Determination of Titration Alkalinity, Marianda) was used to analyze the

DIC samples by coulometric titrations, and the AT by potentiometric titrations (Shadwick et al., 2011a). A calibration of the instrument was performed against certified reference materials (CRM) provided by Andrew Dickson (Scripps Institution of Oceanography) and the reproducibility of the DIC and AT measurements was better than 0.1%.

Each Ra sample (105-215L) was sequentially pre-filtered through 10µm and 1µm filters, either directly using the ship's pump, or a high-volume pump connected to the Niskin bottles. The Ra isotopes were then pre-concentrated by elution through manganese dioxide ($MnO_2$)-coated acrylic fiber cartridges at a constant flow rate of 1 L $min^{-1}$ (Charette et al., 2001; Moore and Reid, 1973; Rutgers van der Loeff and Moore, 1999). To verify the extraction efficiency of the $MnO_2$ fiber cartridge, a second fiber-filter was occasionally mounted in series. $^{224}Ra$ was then determined using a Radium Delayed Coincidence Counter (RaDeCC) (Moore, 2008) that had been calibrated against an IAEA (International Atomic Energy Agency) distributed reference material. The detection limit was estimated to 3 atoms $L^{-1}$ (0.05dpm $100L^{-1}$) for $^{224}Ra$ (see for details Moore, 2008; Moore and Arnold, 1996). No $^{224}Ra$ activity could be detected in any of the second cartridges mounted in series, confirming 100% extraction efficiency. The Mn-fibers were then shipped to the Woods Hole Oceanographic Institution to be ashed at 820°C for 16h, homogenized and transferred to counting vials (Charette et al., 2001). Well-type gamma spectrometers (Canberra and Ortec high purity germanium) were used to quantify $^{226}Ra$ (via $^{214}Pb$ @ 352 keV) and $^{228}Ra$ (via $^{228}Ac$ @ 338 and 911 keV) (International Atomic Energy Agency (IAEA), 2010). Each detector was calibrated with Mn-fiber ash spiked with NIST-certified reference material #4967A ($^{226}Ra$) or a gravimetrically-prepared $Th(NO_3)_4$ solution with the $^{228}Ra$ daughter in secular equilibrium with its parent $^{232}Th$. Detection limits, determined using the Currie Hypothesis test (De Geer, 2004), were determined to be 0.2 dpm for both $^{226}Ra$ and $^{228}Ra$ (Gonneea et al., 2013), which is equivalent to ~0.15 dpm $100L^{-1}$ for a typical 130 L sample.

Barium (Ba) concentrations were determined in water transferred directly from the Niskin bottles to

30mL HDPE plastic bottles containing 15µL of concentrated ultrapure hydrochloric acid (Thomas et al., 2011). Each subsample was then analyzed by Isotope Dilution using Sector Field Inductively Coupled Plasma Mass Spectrometry (SF-ICP-MS, Element 2, Thermo Finnigan) in Brussels. The instrument was run in the low mass resolution mode m/Δm =300. Limit of detection and limit of quantification based on blank analyses were: 0.06 and 0.20 nM, respectively (LOD = 3 X s.d. blank; LOQ =10 X s.d. blank). Reproducibility of multiple measurements of reference materials (SLRS5; SLRS3; OMP) was ≤ 2.5%. Details of the instrument's operational conditions are given by Thomas et al. (2011). The barite saturation state ($Q_i$) is the ratio of the aqueous barium and sulfate ion activity product ($Q_{(BaSO4,\ aq)}$) to the barite solubility product ($K_{Sp}$):

$$Saturation\ State\ BaSO_4(Q_i): = \frac{Q_{BaSO_4aq}}{K_{Sp(Barite)}} \quad \text{(eq. 1)}$$

As described in greater detail by Thomas et al. (2011), $Q_i$ was computed according to Monnin (1999) and Hoppema et al. (2010).

Samples destined for measurements of the stable oxygen isotope composition of seawater ($\delta^{18}O$) were taken directly from the Niskin bottles into 13mL screw-cap plastic test tubes (Lansard et al., 2012). The samples were analyzed at the GEOTOP-UQAM stable isotope laboratory using the $CO_2$ equilibrium method of Epstein and Mayeda (1953) on a Micromass Isoprime universal triple collector isotope ratio mass spectrometer in dual inlet mode (Mucci et al., 2018) at the GEOTOP-UQAM Light Stable Isotope Geochemistry Laboratory. The data were normalized against three internal reference waters, themselves calibrated against Vienna Standard Mean Ocean Water (V-SMOW) and Vienna Standard Light Arctic Precipitation (V-SLAP). Data are reported on the δ-scale in ‰ with respect to V-SMOW, and the average relative standard deviation on replicate measurements is better than 0.05‰.

II.II. Principal Component Analysis

Principal Component Analyses (PCA) were performed to quantitatively determine the correlation between variables as well as the affinity between each of the samples to arbitrary components, while reducing the effects of random variation by using a correlation matrix (Gunasekaran and Kasirajan, 2017; Jolliffe and Cadima, 2016; Pearson, 1901; Peres-Neto et al., 2003). In this study, associated or derived variables such as the radium isotopic ratios were excluded from the PCA due to the congruency with other incorporated variables. Prior to statistical analysis, the variables from each station and depth were transformed to fit a near-normal distribution and normalized to satisfy the parameters of the analysis. Interpolations of the $\delta^{18}O$ and Ba data were made with respect to salinity, as samples were not collected at every depth at each station. The interpolations were verified relative to the original data by means of linear regression and comparison of slopes. Only three surface data samples were interpolated for Ba samples, all from within Baffin Bay. After interpolation and normalization, each sample was categorized by depth: Surface, Middle Depth, Deep Archipelago, or Deep Atlantic, ranging from 0-20m, 21-80m, 81-500m and >500m, respectively.

In addition, quantitative analyses of the PCA results were conducted by a broken stick analysis as a means to distinguish the loading significance of each variable. To this end, eigenvectors were scaled to V-vectors (product of eigenvector multiplied by the square root of the specific eigenvalue) and $V^2$ vectors (V-vectors$^2$) (Jackson, 2004; Peres-Neto et al., 2003). End-members were calculated for each of the variables significantly loading on PC1 from the derived partial values (eigenvector for associated variable multiplied by the PC score for that sample). Each partial value was then de-normalized and back-transformed, thus deriving a refined rendition of the original data set (Appendix 1). Lastly, linear regressions of each variable against the practical salinity were plotted to express robust end-member relationships from within the previously categorized salinity-defined water masses present throughout the CAA. We report the respective end-members as “apparent end-members”, as they resemble the

mean end-member properties in the CAA. For example, an apparent freshwater end-member at null practical salinity ($S_P$=0) would be composed of various individual river and meteoric water end-members, in consideration of their relative weights in this composite. As $^{228}$Ra originates from shelf sediments, which in our study are primarily located in waters at the lower salinity ($S_P \approx 25$) range of the CAA, the $^{228}$Ra end-member was derived from the linear regression to $S_P = 25$ (eg. Rutgers van der Loeff et al., 2003).

## III. Results and Discussion

### III.I. Water Mass Properties

Surface values of $S_p$, density, DIC, AT, and $\delta^{18}O$ were found to increase from west to east through the CAA (Figs. 1, 2a, c, d, f, g, Appendix 2). This trend was extended to the temperature profiles taken throughout the CAA, with the exception of station CAA5, which was found to closely resemble the temperature profile of CAA3 (Fig. 2b, Appendix 2). Prinsenberg and Bennett (1987) reported similar trends employing samples collected in 1982 across Barrow Strait, a sill less than 200m deep located roughly between 105°W to 90°W, where analogous transects for salinity and temperature were recorded throughout the surface layer (Fig. 1). This is both the widest and shallowest section of the CAA. It is responsible for restricting the eastward flow of Deep ATL waters found in the Western Canada Basin and inhibiting high salinity ($S_p > 33.1$) ATL water within Baffin Bay from venturing westward (Hamilton and Wu, 2013; Jones, 2003; Prinsenberg, 1982; Prinsenberg and Bennett, 1987; Shadwick et al., 2011a; Yamamoto-Kawai et al., 2010).

In contrast, dissolved Ba, $^{226}$Ra, and $^{228}$Ra decreased eastward both at the surface as well as at the mid-depth maximum. This is assumed to reflect the elevated flow rates, increasing distance from their source within the CAA, and proximity to the Ba- and $^{228}$Ra-depleted ATL waters in Baffin Bay (Figs. 2e, 3, Appendix 2 and 3) (Thomas et al., 2011). Most often, the $^{228}$Ra/$^{226}$Ra ratio decreases with depth

(Fig. 3c), but occasionally follows a more complex spatial pattern, which will be discussed later.

Positive relationships between DIC and AT vs. $S_p$ (Figs. 4 and 5a for regression intercepts and error) indicate the importance of freshwater inputs from sea-ice melt (SIM) and Meteoric Water (MW, surface runoff and direct precipitation). These freshwater additions contribute to low AT and DIC found in the surface PML waters of the stations west of 96.5°W (Figs. 1, 2, 4, 5c). The highest DIC concentrations were observed at the pycnocline of the western most station (CB4) (Fig. 2, 4, 5a, and Appendix 2). This maximum in metabolic (respiratory) DIC decreased slightly eastward due to the increasing contribution of low-DIC ATL waters (Fig. 5a) (Shadwick et al., 2011a). AT, lacking the metabolic maximum witnessed within the DIC samples, increased linearly with depth and eastward (Figs. 2d, g, 4). This is explained by the concomitant increase in AT and $S_p$ values, rather than a decrease associated with metabolic activity, thus distinguishing AT from DIC (Burt et al., 2016a; Shadwick et al., 2011a; Thomas et al., 2011).

Despite the intrusion of deep Atlantic Ocean waters throughout the CAA (Jones, 2003; Newton and Coachman, 1974), CB4 (in the Canada Basin) displays different ATL, UHL and PML water mass characteristics than those observed at stations within the CAA (Appendix 2 and 3). Hence, for the remainder of this study, we will omit data from CB4 in our discussion of the circulation in the CAA, although we will return to the role and positioning of CB4 in relation to the CAA waters later, particularly in relation to the $^{228}Ra/^{226}Ra$ ratio.

In order to identify water mass distributions and mixing regimes within the CAA, DIC was normalized to a constant salinity ($DIC_{norm}$) (eq. 2). This approach accounts for the influence of fresh water inputs, thereby highlighting possible non-conservative behaviour related to biological processes at the time scale of mixing (Friis et al., 2003; Shadwick et al., 2011b).

$$DIC_{norm} = ((DIC_{measured} - DIC_{S=0}) * S_{measured}^{-1}) * S_{reference} + DIC_{S=0} \quad \text{(eq. 2)}$$

$DIC_{norm}$ decreases eastward in surface waters along the eastward bulk flow throughout the CAA, consistent with observations that surface DIC values were lowest in the western samples (Figs. 1, 2g, h, 5b, c). The reversal in trend reflects the decrease in accumulated respiratory DIC as waters flow eastward through the CAA. The presence of two distinct water masses was highlighted by the $DIC_{norm}$– $S_p$ relationship, distinguishing the surface (PML) from subsurface samples (Figs. 1 and 5c), within each of which mixing processes control the $DIC_{norm}$ distribution. The two water masses themselves, however, hardly mix. A similar water mass grouping has been proposed, based on Ba distributions in waters above and below the UHL (Figs. 2, 5b, c) (Shadwick et al., 2011a; Thomas et al., 2011).

III.II. The use of Radium Isotopes as Water Mass Tracers

Radium isotopes, specifically $^{226}Ra$, $^{228}Ra$ and their ratio ($^{228}Ra/^{226}Ra$), were used as proxies to reconstruct the water mass distribution throughout the CAA. Like the chemical constituents DIC, AT, $\delta^{18}O$ and Ba, as well as the stable oxygen isotopic composition of waters, Ra isotope activity and ratios were found to vary between stations, with depth, as well as across water masses (Appendix 3). The highest $^{228}Ra$ activities were observed at the surface, particularly at the shallow stations 312 and 314, located in the center of the CAA, indicating the $^{228}Ra$ source in coastal sediments (Figs. 1, 6). Lower $^{228}Ra$ activities were found at higher salinities and depths, comparable to values reported by Burt et al. (2016b) in the North Sea, where elevated $^{228}Ra$ activities were present within the shallow, lower salinity waters. Like the $DIC_{norm}$- $S_p$ relationship, the $^{228}Ra$- $S_p$ relationship (Figs. 5b, c, 6) reveals two distinct water masses that distinguish the surface (PML) from subsurface waters. For the surface sample grouping, a negative slope ($^{228}Ra$-$S_P$) was obtained (slope= -2.5x), whereas for the deeper samples a less negative slope was found (slope= -0.5x). The more negative slope, associated with the surface samples collected throughout the CAA, indicates that the system is heavily influenced by the influx of

$^{228}$Ra from the CAA shelf sediments (Fig. 6). In contrast, the slope derived from the $^{228}$Ra activities recorded in the deeper waters of the CAA may imply that these samples originate from an open ocean setting, with minimal (or much less) contact with continental shelf or coastline sediments over the past few decades. As noted earlier (Figs. 3, 6b), the $^{228}$Ra activities decrease from west to east through the CAA in both the surface and deep samples. These values are interpreted as reflecting the mixing of Pacific waters with Atlantic (Baffin Bay) waters east of Barrow Strait. We provide a more detailed analysis of the $^{228}$Ra activity distribution pattern below (section III.III.I.II).

## III.III. Characterizing Water Masses and Isolating End-Members through Principal Component Analysis (PCA)

Further investigation of the dominant water mass patterns was undertaken through Principal Component Analyses (PCA). The first and second principal components (PCs) accounted for 59.1% and 17.5% (total 76.6%), respectively, of the variability in the data (Fig. 7, Table 1). The third PC accounted for a further 13.2% of the variability (89.8% in total). The fourth and fifth PCs together accounted for less than 10% of the variability and were not included in subsequent analyses. PC1, in turn, was inverted to establish apparent end-members of the source waters found in the CAA (section III.III.II.I, see methods II.II).

### III.III.I Qualitative Analysis of PCA

#### III.III.I.I Surface Water Mass Distinction

The first PC (PC1) loaded very heavily on salinity, AT, and $\delta^{18}$O, accounting for 94–97% of the variability in each (see Table 1). It also loaded heavily on DIC and $^{228}$Ra (67% and 66% of variability) and less heavily on Ba (37%). The latter five parameters were all inversely correlated with salinity (Fig. 7). The second PC (PC2) loaded heavily on temperature (83% of variability) and relatively weakly on

DIC (a further 22% of variability for a total of 89% between PC1 and PC2) and Ba (34%, for a total of 71% between PC1 and PC2). There is a correlation between temperature and DIC (Fig. 7), so the component of DIC accounted for by PC2 cannot be ascribed to temperature-dependent solubility. The third PC (PC3), which only accounted for 13.2% of the variability in the data, loaded on $^{226}$Ra (74% of its variability) and was the only PC that did so.

The ordination of samples on PC1 and PC2 shows a strong separation between surface and mid-depth samples vs. deep samples (Fig. 7), reflecting the consistent differences in their parameter values (Figs. 2-6). Variability within surface and subsurface layers was examined by re-running the analysis, using only these data, to minimize the influence by the systematically-different deep-water data on their ordination. The restricted analysis retained most of the parameter relationships observed in the full PCA (Fig. 7, 8). The first PC explained slightly more of the variability (63.5% vs. 59.15%), while the second PC explained slightly less (14.7% vs. 17.5%), for a total of 77.2% vs. 76.7%. There was strong loading of salinity, AT, $\delta^{18}$O, DIC and $^{228}$Ra on PC1, with the latter four being inversely correlated with salinity. In contrast, temperature was strongly correlated with salinity rather than orthogonal to it and Ba was strongly loaded on PC2.

The re-ordination of the surface and mid-depth data indicates a strong geographic separation of the samples on PC1 (Fig. 8), which is also evidenced by temperature-salinity and $^{228}$Ra/$^{226}$Ra-DIC plots (Fig. 9). The first surface group comprises samples from the eastern edge of the CAA, under the influence of Atlantic waters, which enter the CAA via Baffin Bay and Lancaster Sound. The second group comprises the PML-influenced surface samples from the two southern interior CAA stations (312 and 314) and the northwestern CAA stations (CAA4-CAA7), and the mid-water samples (also from stations 312 and 314). It is worth noting that the outer-most surface west samples, likely best visible in the bottom left quadrant of Fig. 9b, came from station CB4. This attribution will be explained later with reference to the apparent end-member properties.

III.III.I.II Distinction of Deep-Water Masses and Indication of Flow

The ordination in the initial PCA is analogous to a T-S diagram, given that PC1 loads on salinity and its covariates and PC2 loads most heavily on temperature. There are very strong similarities between deep-water samples collected in Baffin Bay (Fig. 7; Deep ATL). The deep-water samples within the CAA are ordinated along a gradient between the Deep ATL samples and an end-member that would have negative factor loadings on PC1 and PC2. This would likely be Pacific water. The two deep samples from the westernmost station, CB4, are anomalous (Fig. 7). Their ordination suggests that they are an end-member for the Deep ATL water, likely Deep ATL waters that flow west past Svalbard, before crossing the Lomonosov Ridge and accumulating in the Canada Basin (Coachman and Barnes, 1963; Newton and Coachman, 1974).

Paradoxically, samples collected at Station CAA3 are found at both ends of this trend, having both the highest and lowest similarity to samples collected in the Deep ATL from within the CAA. The three deep-water samples collected at CAA5 are intermediate between the Deep ATL and deep CAA3 waters. The very strong similarity between the deep-water samples collected at CAA3 and those from Baffin Bay indicate that they are ATL water that recirculated counter-clockwise around Baffin Bay, combined with Arctic outflow through Nares Strait (Bâcle et al., 2002; Curry et al., 2011; Lobb et al., 2003). A third PCA was performed excluding the alkalinity (that clearly expresses the bulk eastward flow), to visualize the transition of Deep ATL water as it mixes with the UHL in the CAA (Fig. 10). Results of this analysis reveal that the Deep Arch water mass at stations CAA1, CAA3 and CAA5 are more closely linked to the Deep ATL group, implying that they are in fact part of the Deep ATL water mass (Fig. 10). This suggests that there is an intrusion of ATL water along the northern edge of the CAA. This westward flow with a speed of 2.2 cm/s was observed by Prinsenberg and colleagues (2009) and is weaker than the dominant eastward current flow (15.3 cm/s). This mild inflow of water along the

northern edge of the Archipelago is then assumed to be redirected and exits back to Baffin Bay through the southern Archipelago station (CAA3).

There is further support from observations of dissolved Ba and the barite saturation states ($Q_i$) along the north-to-south transect across the eastern Lancaster Sound (CAA1, CAA2, 323, 324, CAA3) (Fig. 11a, b). An increase in Ba and $Q_i$ was observed from north to south at the surface as well as at depth. Lower Ba concentrations and barite saturation states have been observed in Baffin Bay waters, which are fed by the West Greenland Current. In contrast, the continentally-impacted waters of the CAA are characterized by significantly higher values for the two Ba properties, such that the origin of the waters from the Atlantic and the CAA can clearly be discriminated (Thomas et al., 2011). Furthermore, substantially lower values of the $^{228}Ra/^{226}Ra$ ratio at depth (Fig. 11c) indicate the inflow of Atlantic water on the northern side of Lancaster Sound as well as its outflow along its southern side. Compatibly, the pattern is again revealed by the $^{226}Ra/Ba$ (Fig. 11d), which is dominated by the $^{226}Ra$ variability (Fig 13b,c). The lowest $^{226}Ra/Ba$ value reflects the inflow of low $^{226}Ra$ waters from the Atlantic Ocean (Fig. 11d), as the observed $^{226}Ra$ activities (8-9 dpm $100L^{-1}$, Fig. 3a) are in the same range as those measured in the surface waters of the Atlantic Ocean (Le Roy et al., 2018), part of which feed into the West Greenland Current. Since $^{226}Ra$ activities reveal a much larger north-to-south gradient across Lancaster Sound than Ba does (Figs. 2e, 3a), the discrepancy in the gradients shown in Figs. 11c and 11d is dominated by changes in $^{226}Ra$. The waters transiting through the CAA and exiting on its southern side are enriched with both $^{228}Ra$ and $^{226}Ra$ as they interact with the shallow sediments. The differential half-lives of the two isotopes generate the gradient in the ratio (Figs. 11c, 12) generally revealing higher $^{228}Ra$ fractions the more recent the contact of that particular water mass with shelf sediments. The Ba and Ra data are consistent in revealing the bi-directional flow that links the northern and southern stations along 80°W. This can be attributed to the counter-clockwise, cyclonic circulation found throughout Baffin Bay (Figs. 11, 13, and 14).

A closer look at the $^{226}$Ra-Ba relationship reveals the association between water masses observed in the CAA and those of the surrounding oceans, in particular the Atlantic Ocean (Fig. 13). $^{226}$Ra and Ba appear to vary without an apparent clear relationship. The highest surface values of the $^{226}$Ra/Ba are observed in the interior of the CAA, whereas the lowest are found in the Canada Basin and the eastern side of the CAA (Fig. 13d). The direct relationship between $^{226}$Ra activities and Ba concentrations shows that the Arctic samples with a $S_P > 34$, i.e., waters of Atlantic origin, fall along the relationship established by Le Roy et al. (2018) for the Atlantic, or reported by van Beek et al. (2007) for the Sargasso Sea (Fig. 13a). This relationship, in turn, is similar to the one for the world ocean established from the GEOSECS data-base (Le Roy et al., 2018). This implies that the deep Lancaster Sound samples, as well as the deep Canada Basin samples, can similarly be linked to an Atlantic origin. The remaining CAA samples, with a $S_P < 34$ display a clear deviation from this relationship and towards higher Ba values (Fig. 13b), which can be attributed to the high Ba runoff from rivers draining into the CAA (Guay and Falkner, 1997a). The open-ocean $^{226}$Ra/Ba has been reported to be relatively constant at about 2.2-2.5 dpm ($\mu mol^{-1}$), with elevated values observed only near deep-ocean sediments (van Beek et al., 2007; Le Roy et al., 2018). In contrast, the CAA data show a wider range of $^{226}$Ra/Ba values, which appear to be strongly controlled by the $^{226}$Ra activity, rather than variability of the Ba concentration (Fig. 13b,c). The $^{226}$Ra/Ba in water masses of Atlantic origin ($S_P > 34$) are offset toward higher ratios for a given $^{226}$Ra activity, a consequence of the relatively higher Ba content of the water masses transiting through the CAA. The highest $^{226}$Ra/Ba surface values were observed in the interior of the CAA, whereas the lowest ones were measured in the Canada Basin and the eastern side of the CAA (Fig. 13d).

### III.III.II. Interpretations of PC1 and PC2

#### III.III.II.I. Principal Component One: Advection / Land-Ocean Transition

PC1 was found to correlate significantly with $S_p$, DIC, AT, $\delta^{18}O$, $^{228}Ra$ and Ba, suggesting that this axis represents the land-ocean gradient, i.e., the advective (estuarine) mixing regime of fresh and salt water (Table 1, Fig. 7). This interpretation is consistent with our previous attribution of the longitudinal, eastward increase in $S_p$, DIC, and AT of surface waters through the CAA to a decreasing coastal influence (Figs. 3, 4, 5).

Here, the $^{228}Ra$ activity has to be viewed from a somewhat different perspective, as the sedimentary/shelf sources also reside in the low salinity range of our samples ($S_p$~ 25-30), but does not align with any riverine source (e.g., Rutgers van der Loeff et al., 2003, see below). Therefore, in regards to the PC1 axis, $^{228}Ra$ relative to $^{226}Ra$, represents the coastal, shelf to open ocean transition, decreasing in activity laterally as waters primarily follow the bulk eastward flow and are transported away from the sedimentary source within the CAA (Figs. 12, 13, see also Charette et al., 2016). Accordingly, the fresher $^{228}Ra$ end-member was defined with $S_P = 25$.

The loading of PC1 on $\delta^{18}O$ and Ba is also high, particularly for $\delta^{18}O$. These variables allow us to discriminate between freshwater sources (MW vs. SIM) while also demonstrating a clear mixing gradient along the land-ocean transition (Guay et al., 2009; Macdonald et al., 1999; Yamamoto-Kawai et al., 2010).

We exploit the relationships of salinity to the individual properties derived from PC1 in order to define the freshwater and marine (saline) end-members (Table 2). Again, these end-members should be considered as “apparent”, as these represent observed mean end-member properties, and not end-member water masses, for example, end-members of individual rivers. “Apparent” end-members for each of the significant loading variables associated with PC1 were calculated (Table 2). It should be noted that $^{226}Ra$ was included in the PC1 analysis even though it primarily weighs on the PC3 axis (73.8%), not the PC1 axis. This is because salinity is not a significant loading factor on the PC3 axis (Table 1). Therefore, with the exception of PC3, $^{226}Ra$ most closely associates with the PC1 axis

(18.6%), thus allowing for PC1 to be used to establish the $^{226}Ra$ "mixing" end-member (Table 1).

The computed "apparent" end-members sit along the mixing curve, many located "halfway" between the SIM and MW values reported in the literature (e.g., Cooper et al., 2005; Guay and Falkner, 1998; Macdonald et al., 1989; Shadwick et al., 2011a; Thomas et al., 2011). These "apparent" freshwater end-members ($S_P$=0) thus reflect the combination of freshwater sources. Since both the MW and SIM are equally represented in the "apparent" DIC, AT and Ba end-members, it can be assumed that the freshwater end-member is located within the western portion of the CAA, as the freshwater contribution to the eastern ATL water mass is dominated by SIM, with little to no MW (Shadwick et al., 2011a, 2011b). The "apparent" end-member surface values for $\delta^{18}O$ were found to closely resemble MW (rather than the larger SIM values), with MW being, in essence, the dominant source of freshwater (Table 2) (e.g., Thomas et al., 2011). The end-members associated with the UHL and ATL were also found to be very similar to those reported in the literature, especially AT, Ba, and $\delta^{18}O$ (Guay and Falkner, 1997a, 1997b; Lansard et al., 2012; Macdonald et al., 1989; Shadwick et al., 2011a; Thomas et al., 2011; Yamamoto-Kawai et al., 2010). The "apparent" DIC end-members for these water masses do not closely concur with literature values, nor do those produced here (Fig. 5a), as the DIC end-member associated with the UHL is expected to be larger than that of the ATL (e.g., Lansard et al., 2012; Shadwick et al., 2011a). We argue that this is due to the impact of biological processes, which cannot be resolved solely from mixing-conservative properties. These characteristics will be discussed within the context of PC2 in section III.III.II.II. Furthermore, this result may be due to the normalization required for the PCA linearization of the Deep ATL and Arch samples, thus diminishing the characteristic DIC maximum at the pycnocline. Lastly, we propose apparent end-members for $^{226}Ra$ and $^{228}Ra$ in the CAA. The highest $^{228}Ra$ and $^{226}Ra$ activities were found in the fresh(er) sources attributed to the surface samples collected in the western CAA (Fig. 6). The $S_P$ = 0 end-member for $^{226}Ra$ (25.2 dpm $100L^{-1}$) is consistent with the effective $^{226}Ra$ end-member for the Mackenzie River (26.1 dpm $100L^{-1}$;

Kipp et al., 2019), which contributes to the freshwater budget of the CAA. Smith et al. (2003) reported a Beaufort shelf end-member with a $^{228}$Ra activity of 12 dpm 100L$^{-1}$ at $S_P$= 2 and a $^{228}$Ra/$^{226}$Ra of ~1. Therefore, with a shelf apparent end-member for $^{228}$Ra of 22.4 dpm 100L$^{-1}$ at $S_P$= 25 (Table 2) and a $^{228}$Ra/$^{226}$Ra of ~2, the shelf sediment influence of $^{228}$Ra in the CAA is conclusive.

Similar apparent end-member $^{226}$Ra activities were observed within the open waters of the UHL and ATL, while substantially lower $^{228}$Ra activities were recorded in the ATL (Table 2). Rutgers van der Loeff et al. (2003) reported high-salinity $^{226}$Ra end-members in a similar range (~6-9 dpm 100L$^{-1}$) to the apparent ones reported here, whereas the apparent $^{228}$Ra end-members obtained in our study are clearly lower than those reported by Rutgers van der Loeff et al. (2003, ~3.2-15.4 dpm 100L$^{-1}$). An obvious explanation for this discrepancy may be the circulation history of the respective water masses, as the Atlantic end-member reaches the CAA much later than the Eurasian sector of the Arctic Ocean. Thus the longer circulation history of the ATL waters observed in the CAA allows for a substantial decay of $^{228}$Ra compared to the ATL waters observed on the Eurasian side. Furthermore, the salinity of the samples reported in this study are higher than the samples measured by Rutgers van der Loeff et al. (2003), implying the presence of a stronger ATL component in our samples. The differences between the high salinity apparent $^{226}$Ra and $^{228}$Ra end-members might reflect their vastly different half-lives, allowing for an appreciable decay of $^{228}$Ra at oceanic transport timescales in contrast to the “nearly conservative” $^{226}$Ra. Coinciding with the previous result, higher variability in $^{228}$Ra was seen throughout the water column, whereas $^{226}$Ra activities varied only slightly. Overall, the identification of Ra end-members in the region highlights the Ra sources and transport pathways throughout this complex coastal/shelf environment.

We use the derived apparent end-member properties of $^{228}$Ra and $^{226}$Ra to gain further insight into the distributions of the two isotopes and thus the flow pattern within the CAA. The $^{228}$Ra/$^{226}$Ra was computed as a function of salinity from the apparent end-members and compared to the relationship

between the $^{228}Ra/^{226}Ra$ and $\delta^{18}O$ (Fig. 12a, b). The apparent $^{228}Ra/^{226}Ra$ over $S_P$ mixing ratio appears as if the ratio was only affected by conservative mixing of the two respective end-members (Table 2). When relating this ideal behaviour to the ratios observed in our study, three main groups of samples can be identified. A: the higher salinity ($S_P$>32, $\delta^{18}O$>~-3) samples, that more or less fall together with the mixing relationship. B: the samples characterized by substantially higher $^{228}Ra/^{226}Ra$ (~27<$S_P$<30, ~-5<$\delta^{18}O$<-3), and C: the second group of low-salinity samples with ~$S_P$<31 ($\delta^{18}O$<~-3), characterized by a substantially lower $^{228}Ra/^{226}Ra$ isotopic ratio. The spatial distribution (Fig. 12c) of these sample groups unravels processes that shape the Ra distributions, that, at the first view, did not seem to fit into the broader scheme described in Fig. 9. Samples with higher $^{228}Ra/^{226}Ra$ than the mixing ratios are located within the CAA, at stations 312 and 314, and at the downstream stations along the southern coast of the Northwest Passage, which in turn are under the strong influence of shelf/sediment derived $^{228}Ra$ accumulation as they flow eastward. This water mass mixes on the southern side of Lancaster Sound with the water from Baffin Bay, yielding a flow pattern highlighted by the higher $^{228}Ra/^{226}Ra$ in the CAA (Fig. 11c, 12c). The stations with lower Ra isotopic ratios than the mixing ratios are located on the northern part of the Lancaster Sound and connect to the Canada Basin via McClure Strait and Parry Channel (Figs. 1, 12c). The waters at stations with lower Ra isotopic ratios mix with (inflowing) water from Baffin Bay along the northern side of Lancaster Sound (Fig. 11c). The overall lower $^{228}Ra/^{226}Ra$ waters reflect the long-term isolation of CB4 waters from their margin source (e.g., Kipp et al., 2018) such that the $^{228}Ra$ activities are diminished noticeably by radioactive decay. Consistent with this finding is the clear separation between water of the northern and southern sides of Lancaster Sound, as discussed in Fig. 11. We integrate the observations and findings featured in Figs. 11-13 into a revised scheme, shown in Fig. 14, to reveal the main flow pattern.

This analysis can further be exploited to highlight the release of $^{228}Ra$ from shallow shelf sediments to waters in the lower salinity range rather than from rivers. Both the $^{228}Ra/^{226}Ra$- $S_P$ and $\delta^{18}O$ reveal a

non-conservative addition of $^{228}Ra$ to waters in the salinity range of $25<S_P<30$ (Fig. 12). Furthermore, when considering $\delta^{18}O$, conservative mixing from a riverine source can be excluded (see also Burt et al., 2016b; Kipp et al., 2018; Moore, 2000, 2007). On the other hand, the $\delta^{18}O$ values of -3 to -4 ‰ imply that the $^{228}Ra$ source is under riverine influence, as the $\delta^{18}O$ signature of the sea-ice end-member is generally thought to be approximately -2‰ (e.g., Eicken et al., 2002; Thomas et al., 2011; Yamamoto-Kawai et al., 2009, and references therein, see also Thomas et al., 2011 Fig. 5d).

III.III.II.II: Principal Component Two: Particle-related impacts (nutrient-type behaviour)

The correlation of Ba, DIC and temperature with PC2 is based on the hydrographic peculiarities of the CAA, where temperature displays a “classical”, inverse nutrient-type profile (Fig. 2), resulting from the presence of a temperature minimum in the UHL. As is the case for Ba and DIC, nutrient-type profiles are generally shaped by the interaction of biological (production/respiration, adsorption/desorption) processes and gravitational particle settling. Properties revealing such distributions are represented by PC2, with the temperature minimum coinciding with those minima found at the pycnocline depths.

## IV. Conclusions

It is our hope that with a better understanding of the distributions of the long-lived Ra isotopes, coupled with other chemical constituents, future initiatives can be supported to investigate the changes in water mass distribution in this region. Given the results of the PCA as well as the distribution of $^{228}Ra$, our data reveal the existence of a western flow of water along the northeastern edge of the CAA. This flow is a component of a cyclonic U-turn of Baffin Bay water, intruding westward into the CAA before being rerouted back to the east. The bulk eastward transport of water through the CAA was confirmed, highlighted by the distribution of Ra radioisotopes and chemical constituents in apparent

end-members throughout the region. Overall, the results from this study provide the foundation for future GEOTRACES studies and other initiatives that focus on the sensitivity of trace element fluxes to changing environmental conditions by identifying and quantifying anomalies in the distribution of radioactive isotopes in the Canadian Arctic Archipelago. Furthermore, this study provides an additional tool to better understand and characterize water mass distributions, flow patterns, mixing and their respective time scales in challenging sampling areas such as the Arctic.

**Acknowledgments:**

We wish to thank the captains and crew of the icebreaker CCGS Amundsen as well as the chief scientist, Roger Francois and his team, for their support at sea. We would also like to extend our appreciation to Jacoba Mol and colleagues on the ship for their collaboration. This study was financially supported by the Canadian GEOTRACES program, as part of the NSERC-CCAR initiative. MAC and PBH were supported by U.S. GEOTRACES via the NSF Chemical Oceanography program (#OCE-1458305). FD is grateful to J. Navez, M. Leermakers and K.H. Niroshana for assistance during the Ba analyses in Brussels. HTH acknowledges support by the German Academic Exchange service (DAAD, MOPGA-GRI, #57429828) supported by funds of the German Federal Ministry of Education and Research (BMBF).

**References**

Aagaard, K. and Carmack, E. C.: The Arctic Ocean and Climate: A Perspective, in The Polar Oceans and Their Role in Shaping the Global Environment. (1994), Geophys. Monogr. Ser., vol. 85, edited by O. M. Johannessen, R. D. Muench, and J. E. Overland, pp. 5-20, AGU, Washington, D. C., vol. 85, edited by O. M. Johannessen, R. D. Muench, and J. E. Overland, pp. 5–20, AGU, Washington, DC.

Aagaard, K. and Carmack, E. C.: The role of sea ice and other fresh water in the Arctic circulation, J. Geophys. Res., 94(C10), 14485, doi:10.1029/JC094iC10p14485, 1989.

Aagaard, K., Coachman, L. K. and Carmack, E.: On the halocline of the Arctic Ocean, Deep Sea Res. Part A. Oceanogr. Res. Pap., 28(6), 529–545, doi:10.1016/0198-0149(81)90115-1, 1981.

Bâcle, J., Carmack, E. C. and Ingram, R. G.: Water column structure and circulation under the North Water during spring transition: April–July 1998, Deep Sea Res. Part II Top. Stud. Oceanogr., 49(22–23), 4907–4925, doi:10.1016/S0967-0645(02)00170-4, 2002.

Bauch, D., Schlosser, P. and Fairbanks, R. G.: Freshwater balance and the sources of deep and bottom waters in the Arctic Ocean inferred from the distribution of H218O, Prog. Oceanogr., 35(1), 53–80, doi:10.1016/0079-6611(95)00005-2, 1995.

van Beek, P., Bourquin, M., Reyss, J.-L., Souhaut, M., Charette, M. A. and Jeandel, C.: Radium isotopes to investigate the water mass pathways on the Kerguelen Plateau (Southern Ocean), Deep Sea Res. Part II Top. Stud. Oceanogr., 55(5–7), 622–637, doi:10.1016/J.DSR2.2007.12.025, 2007.

Broecker, W. S., Li, Y. H. and Cromwell, J.: Radium-226 and radon-222: Concentration in Atlantic and Pacific Oceans, Science (80-. )., 158(3806), 1307–1310, doi:10.1126/science.158.3806.1307, 1967.

Burt, W. J., Thomas, H., Hagens, M., Pätsch, J., Clargo, N. M., Salt, L. A., Winde, V. and Böttcher, M. E.: Carbon sources in the North Sea evaluated by means of radium and stable carbon isotope tracers, Limnol. Oceanogr., 61(2), 666–683, doi:10.1002/lno.10243, 2016a.

Burt, W. J., Thomas, H., Miller, L. A., Granskog, M. A., Papakyriakou, T. N. and Pengelly, L.: Inorganic carbon cycling and biogeochemical processes in an Arctic inland sea (Hudson Bay), Biogeosciences, 13(16), 4659–4671, doi:10.5194/bg-13-4659-2016, 2016b.

Charette, M. A., Buesseler, K. O. and Andrews, J. E.: Utility of radium isotopes for evaluating the input and transport of groundwater-derived nitrogen to a Cape Cod estuary, Limnol. Oceanogr., 46(2), 465–470, doi:10.4319/lo.2001.46.2.0465, 2001.

Charette, M. A., Morris, P. J., Henderson, P. B. and Moore, W. S.: Radium isotope distributions during the US GEOTRACES North Atlantic cruises, Mar. Chem., 177, 184–195, doi:10.1016/j.marchem.2015.01.001, 2015a.

Charette, M. A., Morris, P. J., Henderson, P. B. and Moore, W. S.: Radium Isotope Distributions during the US GEOTRACES North Atlantic Cruises, Mar. Chem., doi:10.1016/j.marchem.2015.01.001, 2015b.

Charette, M. A., Lam, P. J., Lohan, M. C., Kwon, E. Y., Hatje, V., Jeandel, C., Shiller, A. M., Cutter, G. A., Thomas, A., Boyd, P. W., Homoky, W. B., Milne, A., Thomas, H., Andersson, P. S., Porcelli, D., Tanaka, T., Geibert, W., Dehairs, F. and Garcia-Orellana, J.: Coastal ocean and shelf-sea biogeochemical cycling of trace elements and isotopes: lessons learned from GEOTRACES, Philos. Trans. R. Soc. A Math. Phys. Eng. Sci., 374(2081), 20160076, doi:10.1098/rsta.2016.0076, 2016.

Chung, Y.: Radium-barium-silica correlations and a two-dimensional radium model for the world ocean, Earth Planet. Sci. Lett., 49(2), 309–318, doi:10.1016/0012-821X(80)90074-6, 1980.

Coachman, L. K. and Aagaard, K.: Physical Oceanography of Arctic and Subarctic Seas, in Marine Geology and Oceanography of the Arctic Seas, pp. 1–72, Springer Berlin Heidelberg, Berlin, Heidelberg., 1974.

Coachman, L. K. and Barnes, C. A.: the Movement of Atlantic Water in the Arctic Ocean, Arctic, 16(1), 1–80, doi:10.14430/arctic3517, 1963.

Cooper, L. W., Benner, R., Mcclelland, J. W., Peterson, B. J., Holmes, R. M., Raymond, P. A., Hansell, D. A., Grebmeier, J. M., Codispoti, L. A., Cooper, L. W., Benner, R., Mcclelland, J. W., Peterson, B. J., Holmes, R. M., Raymond, P. A., Hansell, D. A., Grebmeier, J. M. and Codispoti, L. A.: Linkages among runoff, dissolved organic carbon, and the stable oxygen isotope composition of seawater and other water mass indicators in the Arctic Ocean, J. Geophys. Res, 110, 2013, doi:10.1029/2005JG000031, 2005.

Curry, B., Lee, C. M. and Petrie, B.: Volume, Freshwater, and Heat Fluxes through Davis Strait, 2004-05*, J. Phys. Oceanogr., 11, 429–436, doi:10.1175/2010JPO4536.s1, 2011.

Eicken, H., Krouse, H. R., Kadko, D. and Perovich, D. K.: Tracer studies of pathways and rates of meltwater transport through Arctic summer sea ice, J. Geophys. Res. C Ocean., 107(10), doi:10.1029/2000jc000583, 2002.

Epstein, S. and Mayeda, T.: Variation of O18 content of waters from natural sources, Geochim. Cosmochim. Acta, 4(5), 213–224, doi:10.1016/0016-7037(53)90051-9, 1953.

Friis, K., Körtzinger, A. and Wallace, D. W. R.: The salinity normalization of marine inorganic carbon chemistry data, Geophys. Res. Lett., 30(2), 1–4, doi:10.1029/2002GL015898, 2003.

De Geer, L. E.: Currie detection limits in gamma-ray spectroscopy, in Applied Radiation and Isotopes, vol. 61, pp. 151–160., 2004.

Gonneea, M. E., Mulligan, A. E. and Charette, M. A.: Seasonal cycles in radium and barium within a 3 subterranean estuary: Implications for groundwater 4 derived chemical fluxes to surface waters, Geochim. Cosmochim. Acta, doi:10.1016/j.gca.2013.05.034, 2013.

Guay, C. K. and Falkner, K.: A survey of dissolved barium in the estuaries of major Arctic rivers and adjacent seas, Cont. Shelf Res., 18, 859–882, 1997a.

Guay, C. K. and Falkner, K. K.: Barium as a tracer of Arctic halocline and river waters, in Deep-Sea Research Part II: Topical Studies in Oceanography, vol. 44, pp. 1543–1559., 1997b.

Guay, C. K. H., Mclaughlin, F. A. and Yamamoto-Kawai, M.: Differentiating fluvial components of upper Canada Basin waters on the basis of measurements of dissolved barium combined with other physical and chemical tracers, J. Geophys. Res., 114, doi:10.1029/2008JC005099, 2009.

Gunasekaran, R. and Kasirajan, T.: Principal Component Analysis (PCA) for Beginners, Int. J. Adv. Sci. Res. Manag., 2(9), 9–11, 2017.

Hamilton, J. and Wu, Y.: Synopsis and trends in the physical environment of Baffin Bay and Davis

Strait, Can. Tech. Rep. Hydrogr. Ocean Sci., 282(282), 1–39, 2013.

Hamilton, J., Collins, K. and Prinsenberg, S. J.: Links between ocean properties, ice cover, and plankton dynamics on interannual time scales in the Canadian Arctic Archipelago, J. Geophys. Res. Ocean., 118(10), 5625–5639, doi:10.1002/jgrc.20382, 2013.

Holland, M. M., Bitz, C. M., Eby, M. and Weaver, A. J.: The role of ice-ocean interactions in the variability of the North Atlantic thermohaline circulation, J. Clim., 14(5), 656–675, doi:10.1175/1520-0442(2001)014<0656:TROIOI>2.0.CO;2, 2001.

Hoppema, M., Dehairs, F., Navez, J., Monnin, C., Jeandel, C., Fahrbach, E. and de Baar, H. J. W.: Distribution of barium in the Weddell Gyre: Impact of circulation and biogeochemical processes, Mar. Chem., 122(1–4), 118–129, doi:10.1016/j.marchem.2010.07.005, 2010.

Ingram, R. G. and Prinsenberg, S. J.: Coastal oceanography of Hudson Bay and surrounding eastern Canadian Arctic Waters Coastal Segment (26P), in The Sea, vol. 11, edited by A. R. Robinson and K. H. Brink, pp. 835–861, Wiley, New York., 1998.

International Atomic Energy Agency (IAEA): Inventories of Selected Radionoclides in the Oceans, Vienna., 1988.

International Atomic Energy Agency (IAEA): Analytical Methodology for the Determination of Radium Isotopes in Environmental Samples (IAEA/AQ--19), Seiberdorf (Austria)., 2010.

Jackson, J. E.: Scaling of Data, pp. 63–79, John Wiley & Sons, Ltd., 2004.

Jakobsson, M.: Hypsometry and volume of the Arctic Ocean and its constituent seas, Geochemistry, Geophys. Geosystems, 3(5), 1–18, doi:10.1029/2001GC000302, 2002.

Jolliffe, I. T. and Cadima, J.: Principal component analysis: a review and recent developments., Philos. Trans. A. Math. Phys. Eng. Sci., 374(2065), 20150202, doi:10.1098/rsta.2015.0202, 2016.

Jones, E. P.: Tracing Pacific water in the North Atlantic Ocean, J. Geophys. Res., 108(C4), 3116, doi:10.1029/2001JC001141, 2003.

Kadko, D. and Muench, R.: Evaluation of shelf-basin interaction in the western Arctic by use of short-lived radium isotopes: The importance of mesoscale processes, Deep. Res. Part II Top. Stud. Oceanogr., 52(24–26), 3227–3244, doi:10.1016/j.dsr2.2005.10.008, 2005.

Kawakami, H. and Kusakabe, M.: Surface water mixing estimated from 228Ra and 226Ra in the northwestern North Pacific, J. Environ. Radioact., 99(8), 1335–1340, doi:10.1016/j.jenvrad.2008.04.011, 2008.

Kipp, L. E., Charette, M. A., Moore, W. S., Henderson, P. B. and Rigor, I. G.: Increased fluxes of shelf-derived materials to the central Arctic Ocean, Sci. Adv., 4(January), 1–9, doi:10.1126/sciadv.aao1302, 2018.

Kipp, L. E., Kadko, D. C., Pickart, R. S., Henderson, P. B., Moore, W. S. and Charette, M. A.: Shelf-Basin Interactions and Water Mass Residence Times in the Western Arctic Ocean: Insights Provided by Radium Isotopes, J. Geophys. Res. Ocean., 124(5), 3279–3297, doi:10.1029/2019JC014988, 2019.

Lansard, B., Mucci, A., Miller, L. A., Macdonald, R. W. and Gratton, Y.: Seasonal variability of water mass distribution in the southeastern Beaufort Sea determined by total alkalinity and $\delta^{18}$O, J. Geophys. Res. Ocean., 117(C3), n/a-n/a, doi:10.1029/2011JC007299, 2012.

Lobb, J., Carmack, E. C., Ingram, R. G. and Weaver, A. J.: Structure and mixing across an Arctic/Atlantic front in northern Baffin Bay, Geophys. Res. Lett., 30(16), doi:10.1029/2003GL017755, 2003.

Macdonald, R. W., Wong, C. S. and Erickson, P. E.: The distribution of nutrients in the southeastern Beaufort Sea: Implications for water circulation and primary production, J. Geophys. Res., 92(C3), 2939, doi:10.1029/JC092iC03p02939, 1987.

Macdonald, R. W., Carmack, E. C., McLaughlin, F. A., Iseki, K., Macdonald, D. M. and O'Brien, M. C.: Composition and modification of water masses in the Mackenzie shelf estuary, J. Geophys. Res., 94(C12), 18057, doi:10.1029/JC094iC12p18057, 1989.

Macdonald, R. W., Carmack, E. C., Mclaughlin, F. A., Falkner, K. K. and Swift, J. H.: Connections among ice, runoff and atmospheric forcing in the Beaufort Gyre, Geophys. Res. Lett., 26(15), 2223–2226, doi:10.1029/1999GL900508, 1999.

Mathis, J. T., Hansell, D. A. and Bates, N. R.: Strong hydrographic controls on spatial and seasonal variability of dissolved organic carbon in the Chukchi Sea, Deep Sea Res. Part II Top. Stud. Oceanogr., 52(24–26), 3245–3258, doi:10.1016/J.DSR2.2005.10.002, 2005.

Monnin, C.: A thermodynamic model for the solubility of barite and celestite in electrolyte solutions and seawater to 200°C and to 1 kbar, Chem. Geol., 153(1–4), 187–209, doi:10.1016/S0009-2541(98)00171-5, 1999.

Moore, W. S.: Determining coastal mixing rates using radium isotopes, Cont. Shelf Res., 20(15), 1993–2007, doi:10.1016/S0278-4343(00)00054-6, 2000.

Moore, W. S.: Seasonal distribution and flux of radium isotopes on the southeastern U.S. continental shelf, , doi:10.1029/2007JC004199, 2007.

Moore, W. S.: Fifteen years experience in measuring 224Ra and 223Ra by delayed-coincidence counting, Mar. Chem., 109(3–4), 188–197, doi:10.1016/j.marchem.2007.06.015, 2008.

Moore, W. S. and Arnold, R.: Measurement of 223 Ra and 224 Ra in coastal waters using a delayed coincidence counter, J. Geophys. Res. Ocean., 101(C1), 1321–1329, doi:10.1029/95JC03139, 1996.

Moore, W. S. and Dymond, J.: Fluxes of 226Ra and barium in the Pacific Ocean: The importance of boundary processes, Earth Planet. Sci. Lett., 107(1), 55–68, doi:10.1016/0012-821X(91)90043-H, 1991.

Moore, W. S. and Reid, D. F.: Extraction of Radium from Natural Waters Using Manganese-Impregnated Acrylic Fibers, J. Geophys. Res. DECEMBER, 78(20), doi:10.1029/JC078i036p08880, 1973.

Moore, W. S., Feely, H. W. and Li, Y.-H.: Radium isotopes in sub-Arctic waters, Earth Planet. Sci.

Lett., 49(2), 329–340, doi:10.1016/0012-821X(80)90076-X, 1980.

Moore, W. S., Sarmiento, J. L. and Key, R. M.: Submarine groundwater discharge revealed by 228Ra distribution in the upper Atlantic Ocean, , doi:10.1038/ngeo183, 2008.

Mucci, A., Levasseur, M., Gratton, Y., Martias, C., Scarratt, M., Gilbert, D., Tremblay, J.-É., Ferreyra, G. and Lansard, B.: Tidally induced variations of pH at the head of the Laurentian Channel, Can. J. Fish. Aquat. Sci., 75(7), 1128–1141, doi:10.1139/cjfas-2017-0007, 2018.

Newton, J. L. and Coachman, L. K.: Atlantic Water Circulation in the Canada Basin, Arctic, 27(4), 297–303, doi:10.2307/40508628, 1974.

Pearson, K.: On lines and planes of closet fit to systems of points in space., J. Sci., 2(11), 559–572, doi:10.1080/14786440109462720, 1901.

Peres-Neto, P. R., Jackson, D. a and Somers, K. M.: Giving meaningful interpritation to ordination axes: Assesing loading significance in principal components analysis, Ecology, 84(9), 2347–2363, doi:10.1890/00-0634, 2003.

Peterson, I., Hamilton, J., Prinsenberg, S. and Pettipas, R.: Wind-forcing of volume transport through Lancaster Sound, J. Geophys. Res. Ocean., 117(11), doi:10.1029/2012JC008140, 2012.

Prinsenberg, S., Hamilton, J., Peterson, I. and Pettipas, R.: Observing and interpreting the seasonal variability of the oceanographic fluxes passing through Lancaster Sound of the Canadian Arctic Archipelago, in Influence of Climate Change on the Changing Arctic and Sub-Arctic Conditions, pp. 125–143, Springer Netherlands., 2009.

Prinsenberg, S. J.: Volume, Heat and freshwater flxes through the Canadian Arctic Archipelago: Present Understanding and Future Research Plans., Bedford Inst. Ocean., 1982.

Prinsenberg, S. J. and Bennett, E. B.: Mixing and transports in Barrow Strait, the central part of the Northwest Passage, Cont. Shelf Res., 7(8), 913–935, doi:https://doi.org/10.1016/0278-4343(87)90006-9, 1987.

Rahmstorf, S.: Ocean circulation and climate during the past 120,000 years, Nature, 419(6903), 207–214, doi:https://doi.org/10.1038/nature01090, 2002.

Le Roy, E., Sanial, V., Charette, M. A., Van Beek, P., Lacan, F., Jacquet, H. M. S., Henderson, P. B., Souhaut, M., García-Ibáñez, M. I., Jeandel, C., Pérez, F. F. and Sarthou, G.: The 226Ra-Ba relationship in the North Atlantic during GEOTRACES-GA01, Biogeosciences, 15(9), 3027–3048, doi:10.5194/bg-15-3027-2018, 2018.

Rudels, B.: The outflow of polar water through the Arctic Archipelago and the oceanographic conditions in Baffin Bay, Polar Res., 4(2), 161–180, doi:https://doi.org/10.3402/polar.v4i2.6929, 1986.

Rutgers van der Loeff, M. and Moore, W.: Methods of seawater analysis, 3rd ed., edited by B. B. Leif G. Anderson, Meinrat 0. Andreae, K. A. B. Constant van den Berg, Lutz Brugmann, M. E. Gustave Cauwet, Jan C. Duinker, David Dyrssen, H. P. H. Elisabet Fogelqvist, Stig Fonselius, F. K. Arne Kortzinger, Wolfgang Koeve, W. S. M. Klaus Kremling, Joachim Kuss, Gerd Liebezeit, M. R. van der L. Thomas J. Miiller, Andreas Prange, P. J. S. Martina Schirmacher, Detlef Schulz-Bull, P. W. David R. Turner, Gunther Uher, and B. Y. Margareta Wedborg, Peter J. le B. Williams, WILEY-VCH, Kiel., 1999.

Rutgers Van Der Loeff, M., Kühne, S., Wahsner, M., Höltzen, H., Frank, M., Ekwurzel, B., Mensch, M. and Rachold, V.: 228Ra and 226Ra in the Kara and Laptev seas, Cont. Shelf Res., 23(1), 113–124, doi:10.1016/S0278-4343(02)00169-3, 2003.

Rutgers Van Der Loeff, M. M., Key, R. M., Scholten, J., Bauch, D. and Michel, A.: 228Ra as a tracer for shelf water in the arctic ocean, Deep. Res. Part II, 42(6), 1533–1553, doi:10.1016/0967-0645(95)00053-4, 1995.

Shadwick, E. H., Thomas, H., Gratton, Y., Leong, D., Moore, S. A., Papakyriakou, T. and Prowe, A. E. F.: Export of Pacific carbon through the Arctic Archipelago to the North Atlantic, Cont. Shelf Res., 31, 806–816, doi:10.1016/j.csr.2011.01.014, 2011a.

Shadwick, E. H., Thomas, H., Chierici, M., Else, B., Fransson, A., Michel, C., Miller, L. A., Mucci, A., Niemi, A., Papakyriakou, T. N. and Tremblay, J.-É.: Seasonal variability of the inorganic carbon system in the Amundsen Gulf region of the southeastern Beaufort Sea, Limnol. Oceanogr., 56(1), 303–322, doi:10.4319/lo.2011.56.1.0303, 2011b.

Shadwick, E. H., Trull, T. W., Thomas, H. and Gibson, J. A. E.: Vulnerability of Polar Oceans to Anthropogenic Acidification: Comparison of Arctic and Antarctic Seasonal Cycles, Sci. Rep., 3(2339), 1–7, doi:10.1038/srep02339, 2013.

Smith, J. ., Moran, S. . and Macdonald, R. .: Shelf–basin interactions in the Arctic Ocean based on 210Pb and Ra isotope tracer distributions, Deep Sea Res. Part I Oceanogr. Res. Pap., 50(3), 397–416, doi:10.1016/S0967-0637(02)00166-8, 2003.

Thomas, H., Shadwick, E., Dehairs, F., Lansard, B., Mucci, A., Navez, J., Gratton, Y., Prowe, F., Chierici, M., Fransson, A., Papakyriakou, T. N., Sternberg, E., Miller, L. A., Tremblay, J. É. and Monnin, C.: Barium and carbon fluxes in the Canadian Arctic Archipelago, J. Geophys. Res., 116, 1–16, doi:10.1029/2011JC007120, 2011.

Walsh, J. J.: Importance of continental margins in the marine biogeochemical cycling of carbon and nitrogen, Nature, 350, 53–55, doi:https://doi.org/10.1038/350053a0, 1991.

Wang, Q., Myers, P. G., Hu, X. and Bush, A. B. G.: Flow Constraints on Pathways through the Canadian Arctic Archipelago, , doi:10.1080/07055900.2012.704348, 2012.

Xing, N., Chen, M., Huang, Y., Cai, P. and Qiu, Y.: Distribution of 226Ra in the Arctic Ocean and the Bering Sea and its hydrologic implications, Sci. China Ser. D, 46(5), 516, doi:10.1360/03yd9045, 2003.

Yamamoto-Kawai, M., Mclaughlin, F. A., Carmack, E. C., Nishino, S., Shimada, K. and Kurita, N.: Surface freshening of the Canada Basin, J. Geophys. Res, 114, 0–05, doi:10.1029/2008JC005000, 2009.

Yamamoto-Kawai, M., Carmack, E. C., McLaughlin, F. a. and Falkner, K. K.: Oxygen isotope ratio,

barium and salinity in waters around the North American coast from the Pacific to the Atlantic: Implications for freshwater sources to the Arctic throughflow, J. Mar. Res., 68(1), 97–117, doi:10.1357/002224010793078988, 2010.

**Figure Captions:**

**Figure 1:** Map of the Canadian Arctic Archipelago (CAA) showing the 17 stations sampled during the 2015 GEOTRACES cruise aboard the CCGS Amundsen (red dots), where the two unlabeled stations along the Eastern CAA cross-channel transect are the surface stations 323 and 324, numbers refer to CAA stations (1-7). Nares Strait (NS), Barrow Strait (BS), McClure Strait (McS), Lancaster Sound (LS) and Parry Channel (PC) are denoted, the latter connecting the CAA from McS via BS to LS. Underway (UW) samples have been taken on the way from Baffin Bay (BB) into Lancaster Sound. Lastly, the blue and grey lines indicate the 200m and 100m isobaths, respectively.

**Figure 2:** Vertical distributions of practical salinity, temperature, density, AT, Ba, $\delta^{18}O$, DIC and normalized DIC ($DIC_{norm}$) observed at stations CAA1 to CAA7 throughout the CAA.

**Figure 3:** $^{226}Ra$ (a), $^{228}Ra$ (b) and $^{228}Ra/^{226}Ra$ (c) profiles ranging from surface to depth for stations CAA1 to CAA7 (where pink dots indicate station CAA2 which was only sampled at the surface and bottom) throughout the Canadian Arctic Archipelago.

**Figure 4**: Total Alkalinity (AT) versus salinity measured throughout the CAA with coloured depth (a) and longitude (b). A linear regression analysis yields $AT = 52.7*S_P+492.3$ ($R^2=0.91$).

**Figure 5:** Dissolved Inorganic Carbon (DIC) (a) and salinity-normalized Dissolved Inorganic Carbon ($DIC_{norm}$) (b) were plotted against salinity ($S_p$), with colours indicating depth (m) (a, b) and longitude (c). The DIC vs. $S_p$ regression yields $DIC=(53.4\pm2.8)*S_p+371\pm89$ ($R^2 = 0.86$). The $DIC_{norm}$ vs. $S_p$ plots were fitted with a piecewise regression analysis representing the surface, $DIC_{norm}=(-19.7\pm3.9)*S_p+2681\pm120$ ($R^2=0.5$) and at depth; $DIC_{norm}=(-34.2\pm3.5)*S_p+3282\pm117$ ($R^2=0.76$). In plots b & c CB4 was excluded from the piecewise regression (represented by unfilled,

crossed out grey circles), whereas stations 312 and 314 surface samples were excluded entirely. The black diamonds identify the average Atlantic deep-water samples from stations CAA1, CAA2 and CAA3.

**Figure 6:** $^{228}$Ra (dpm/100L) plotted against practical salinity with colour indicating depth (a) and longitude (b) fitted with a piecewise regression excluding the deep stations of the Canada Basin (grey circles) and yielding $^{228}Ra = (-2.5\pm0.8)*S_p + 86.4\pm23.6$ ($R^2 = 0.28$) for the surface trend (0-80m) and $^{228}Ra = (-0.5\pm0.3)*S_p + 21.1\pm10.5$ ($R^2 = 0.07$) for the deep trend (>80m). The average of Atlantic deep waters sampled from stations CAA1, CAA2 and CAA3 is defined by a black diamond."

**Figure 7:** Eight-variable Principal Component Analysis (PCA) of PC1 and PC2 for 64 samples from 17 stations throughout the Canadian Arctic Archipelago, distinguished by depth groupings; Surface (0-20m; purple), Mid (20-80m; blue), Deep (Deep Arch, 80-500m; red) Archipelago and Deep Atlantic (Deep ATL, >500m; green). The sample collected at station CB4 at 200m depth was excluded from this plot. The ellipses represent 95% confidence intervals associated with each water mass grouping.

**Figure 8:** Eight-variable Principal Component Analysis of surface samples (0-20m;) east (green, east of 85°W) and west (blue, west of 85°W) and mid-Depth (20-80m; red) samples collected throughout the Canadian Arctic Archipelago analyzing PC1 and PC2 for 27 samples from 17 stations, with the exception of the surface sample collected at station CB4 that was excluded from this plot. The ellipses represent 95% confidence intervals associated with each water mass grouping.

**Figure 9:** Temperature-Salinity plots with colours indicating depth (a) and longitude (b) as well as the Radium Isotopic Ratio($^{228}$Ra/$^{226}$Ra)-DIC plots with colour indicating depth (c) and Salinity (d), highlighting three water masses throughout the CAA, the two surface water masses the Western Surface (Surf W) and Eastern Surface (Surf E) waters and one water mass (Atlantic) at depth (Deep). In (c) and (d) station CB4 has been denoted with a circle and cross.

**Figure 10:** Principal Component Analysis (PCA) of PC1 and PC2 for 64 samples from 17 stations

throughout the Canadian Arctic Archipelago, composed of the seven normalized variables Salinity ($S_P$), Temperature (T), DIC, Ba, $\delta^{18}O$, $^{228}Ra$, and $^{226}Ra$, excluding AT. They are distinguished by depth groupings; Surface (0-20m; purple), Mid (20-80m; blue), Deep (Deep Arch, 80-500m; red) Archipelago and Deep Atlantic (Deep ATL, >500m; green).

**Figure 11:** Cross section at stations CAA1-3, 323 and 324 for dissolved Ba (a) and barite saturation state ($Q_i$) (b), as well as $^{228}Ra/^{226}Ra$ (c) and $^{226}Ra$/Ba (dpm µmol$^{-1}$) (d). The low values of both properties indicate the presence of Atlantic water (see Thomas et al., 2011).

**Figure 12:** Relationship between the $^{228}Ra/^{226}Ra$ as derived from the apparent end-members vs. salinity (a) and $\delta^{18}O$ (b). In insert in (a), the $S_P$ vs. $\delta^{18}O$ relationship. Increasing fractions of sea-ice would cause a near-horizontal shift in that relationship (sea-ice $\delta^{18}O$ end-member = -2‰), whereas meteoric water would cause a "diagonal" shift (meteoric water $\delta^{18}O$ end-member = -20‰); see also Thomas et al., 2011 for more details. $^{228}Ra/^{226}Ra$ in surface samples across the CAA depict the different flow pass via the CAA/northwest passage, and via McClure Strait, Parry Channel and Lancaster Sound (c). For reasons of clarity, only the surface samples have been shown in (c). The colour coding groups the samples into water masses with high salinity and low isotopic ratio (ATL), with low salinity and high isotopic ratio (shelf waters near the $^{228}Ra$ source), and lastly with low salinity and low isotopic ratio (waters in direction of CB4), respectively.

**Figure 13:** Relationships between $^{226}Ra$ and Ba (a), and between the $^{226}Ra$/Ba and $^{226}Ra$ and Ba concentrations (b), respectively (c). The red symbols indicate samples with $S_P$>34 (Atlantic origin). In (b) the linear regressions yield for samples with $S_P$>34 $f(x) = 0.20x + 0.25$, $R^2$=0.99, and $S_P$<34 $f(x) = 0.18x + 0.05$, $R^2$=0.90. Within (a) and (b), open circles are drawn from van Beek et al., (2007), whereas

the dashed line in (a) is redrawn from Le Roy et al., (2018). Panel (d) depicts the spatial distribution of the $^{226}Ra/Ba$ in surface waters across the CAA.

**Figure 14:** Sketch of proposed surface flow pattern as identified in the current study where dotted lines indicated reduced certainty of trends.

## Appendices:

**Appendix 1:** Equations used to normalize ($X_0$) the data distribution for Temperature, Salinity, Dissolved Inorganic Carbon (DIC, µmol/kg), $\delta^{18}O$, $^{226}Ra$ (dpm/100L), $^{228}Ra$ (dpm/100L) and Ba (nM) collected throughout the CAA 2015 GEOTRACES cruise in preparation for Principal Component Analyses.

**Appendix 2:** DIC (µmol/kg), AT (µmol/kg), $\delta^{18}O$, and Ba (nM) plotted against depth for each station including CAA1, CAA2, CAA3, CAA4, CAA5. CAA6, CB4, 312, and 314, where profiles were taken throughout the 2015 GEOTRACES cruise in the Canadian Arctic Archipelago. Colours indicate the water masses present at the sampled depth; red is the Polar Mixed Layer (PML), yellow is the Upper Halocline Layer (UHL), and blue is the Atlantic Layer (ATL).

**Appendix 3:** $^{226}Ra$ (dpm/100L), $^{228}Ra$ (dpm/100L), and Ra isotopic ratio ($^{228}Ra/^{226}Ra$) plotted against depth for each station, including CAA1, CAA2, CAA3, CAA4, CAA5, CAA6, and CAA7, where profiles were taken throughout the 2015 GEOTRACES cruise in the Canadian Arctic Archipelago. Colours of depth indicate water masses at the sampled depths; red is the Polar Mixed Layer (PML), yellow is the Upper Halocline Layer (UHL), and blue is the Atlantic Layer (ATL).

**Table 1** Eigenvalues and Normalized $V^2$ Vectors for Temperature, Salinity, Dissolved Inorganic Carbon (DIC), Total Alkalinity (AT), $\delta^{18}O$, $^{226}Ra$, $^{228}Ra$ and Barium (Ba), where bolded values represent significant weight attributed to that Principal Component (where PC 4 and 5 were not analyzed, shaded) derived from the original 8-variable PCA (Fig. 7).

| PC | Eigenvalues | Temperature | Salinity | DIC | AT | $\delta^{18}O$ | $^{226}Ra$ | $^{228}Ra$ | Ba |
|---|---|---|---|---|---|---|---|---|---|
| 1 | 4.74 | 0.007 | **0.968** | **0.666** | **0.947** | **0.939** | 0.186 | **0.656** | **0.372** |
| 2 | 1.41 | **0.834** | 0 | **0.224** | 0.008 | 0.003 | 0 | 0 | **0.34** |
| 3 | 1.03 | 0 | 0.022 | 0.046 | 0.006 | 0.038 | **0.738** | 0.154 | 0.027 |
| 4 | 0.486 | 0.135 | 0 | 0.004 | 0.009 | 0 | 0.03 | 0.059 | **0.248** |
| 5 | 0.246 | 0.024 | 0.001 | 0.038 | 0.002 | 0 | 0.043 | 0.128 | 0.009 |

**Table 2** Apparent Dissolved Inorganic Carbon (DIC, µmol/kg), Total Alkalinity (AT, µmol/kg), $\delta^{18}O$, Barium (Ba, nM), $^{226}Ra$ (dpm/100L), and $^{228}Ra$ (dpm/100L) end members, analyzed for the salinity (S) defined water masses Sea Ice Melt and Melt Water (SIM & MW), Upper Halocline Layer (UHL) and the Atlantic Layer (ATL) from PC1 of the original 8-variable PCA (Fig. 7) with exception to $^{226}Ra$, which does not significantly coincide with PC1.

| Water Mass | S | DIC | AT | $\delta^{18}O$ | Ba | $^{226}Ra$ | $^{228}Ra$ |
|---|---|---|---|---|---|---|---|
| SIM & MW | 0 | 607 | 648 | -18.9 | 105 | 25.2 | |
| Shelf | 25 | | | | | | 22.4 |
| UHL | 33.1 | 2145 | 2282 | -1.18 | 50.8 | 10.6 | 5.3 |
| ATL | 35 | 2233 | 2375 | -0.157 | 47.7 | 9.8 | 1.3 |

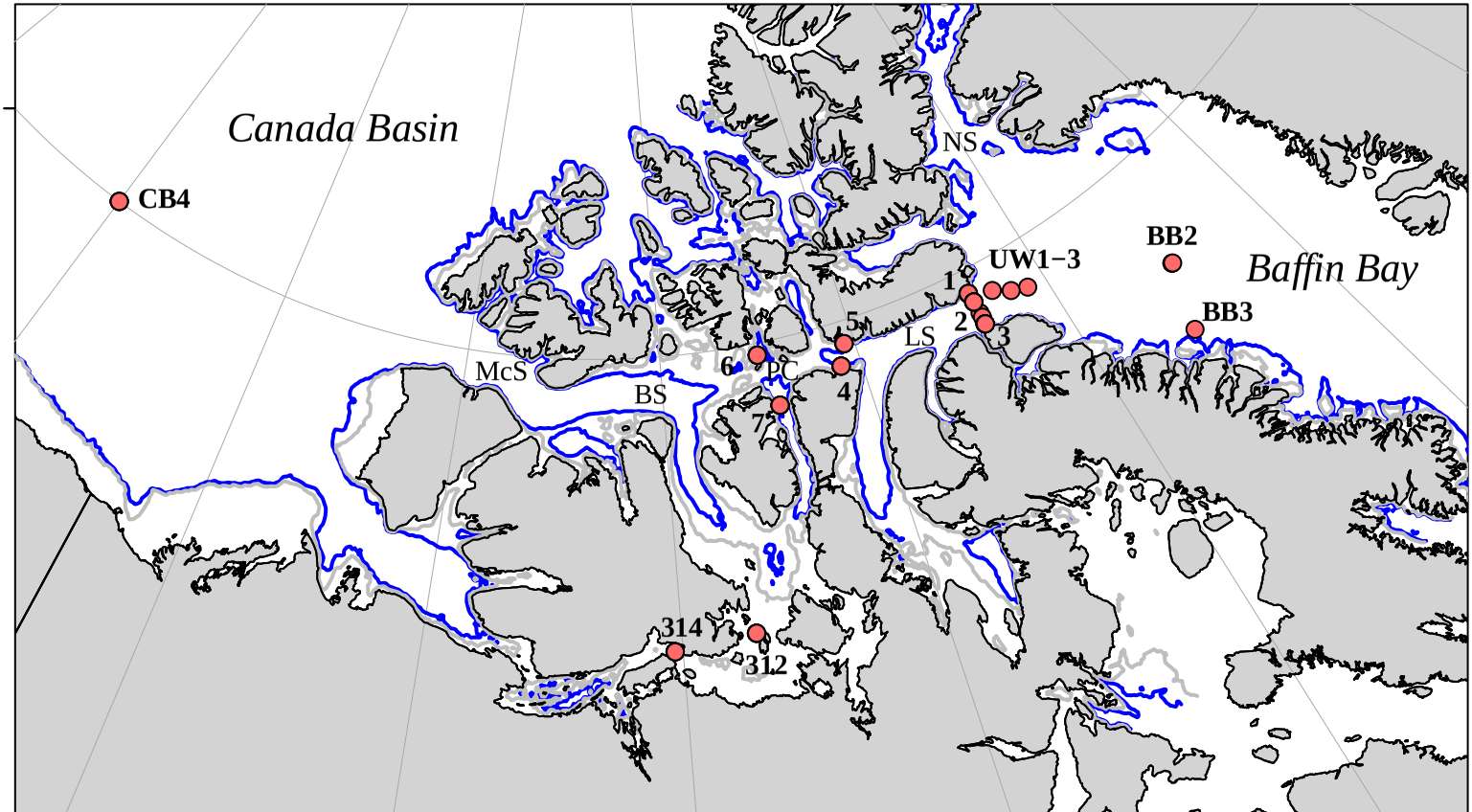
Canada Basin
Baffin Bay
CB4
BB2
BB3
UW1–3
1
2
3
4
5
6
7
LS
NS
McS
BS
DC
314
312
75N
135W
120W
105W
90W
75W

Figure 1

Figure 2

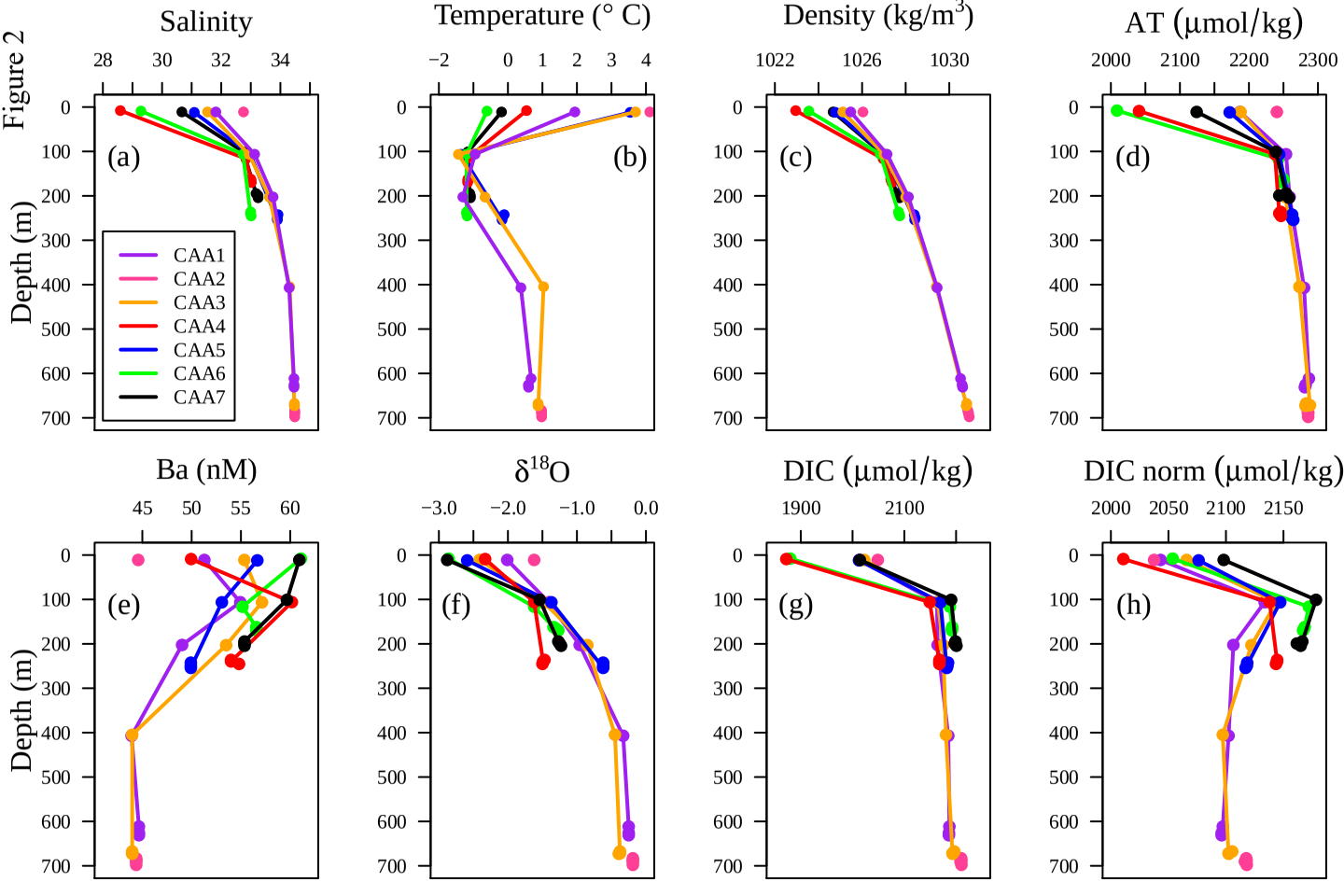
Salinity
28
30
32
34
Temperature (° C)
−2
0
1
2
3
4
Density (kg/m$^3$)
1022
1026
1030
AT (µmol/kg)
2000
2100
2200
2300
Ba (nM)
45
50
55
60
δ$^{18}$O
−3.0
−2.0
−1.0
0.0
DIC (µmol/kg)
1900
2100
DIC norm (µmol/kg)
2000
2050
2100
2150
Depth (m)
0
100
200
300
400
500
600
700
(a)
(b)
(c)
(d)
(e)
(f)
(g)
(h)
CAA1
CAA2
CAA3
CAA4
CAA5
CAA6
CAA7

Figure 3

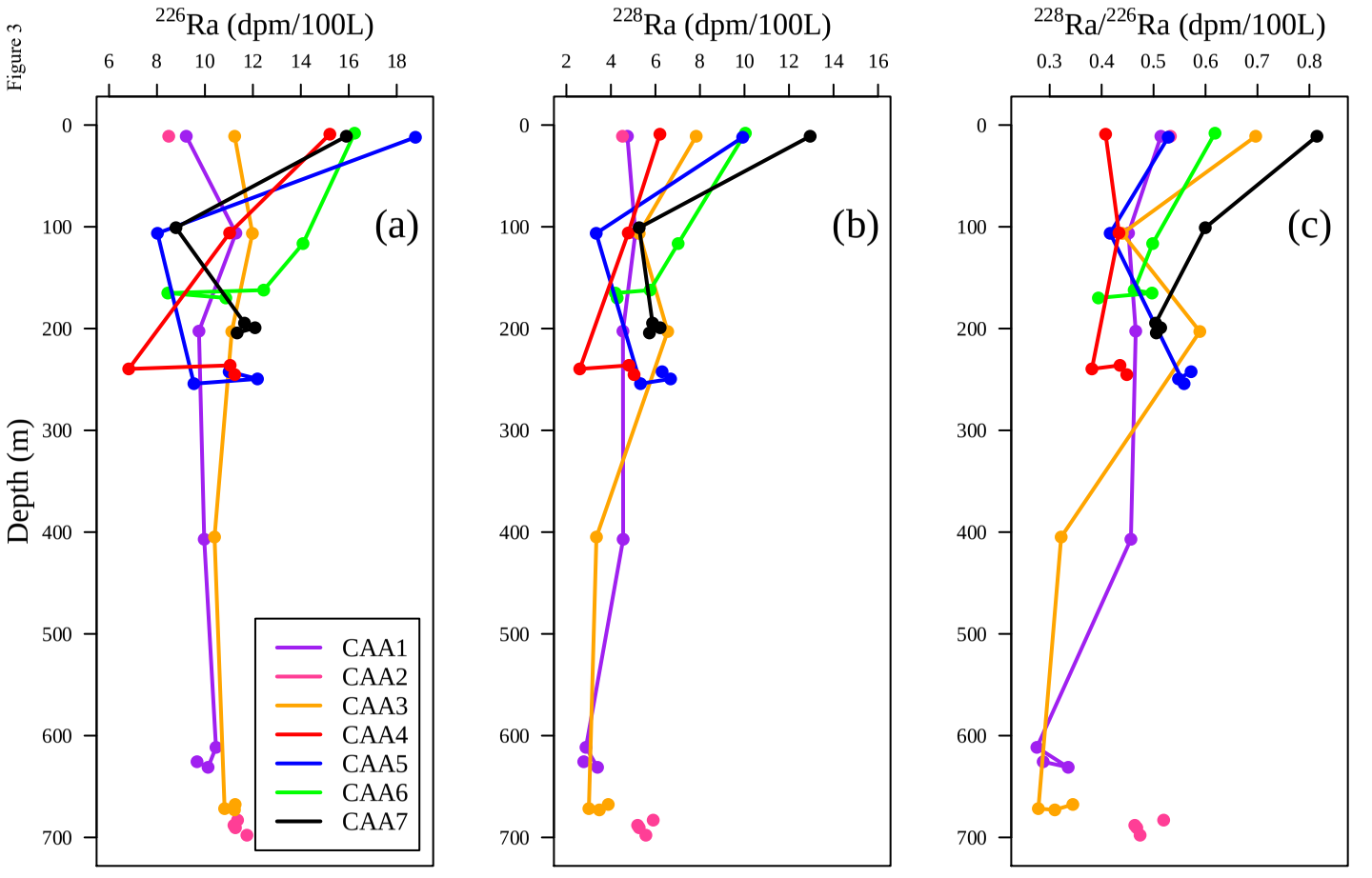
226Ra (dpm/100L)
228Ra (dpm/100L)
228Ra/226Ra (dpm/100L)
Depth (m)
(a)
(b)
(c)
CAA1
CAA2
CAA3
CAA4
CAA5
CAA6
CAA7

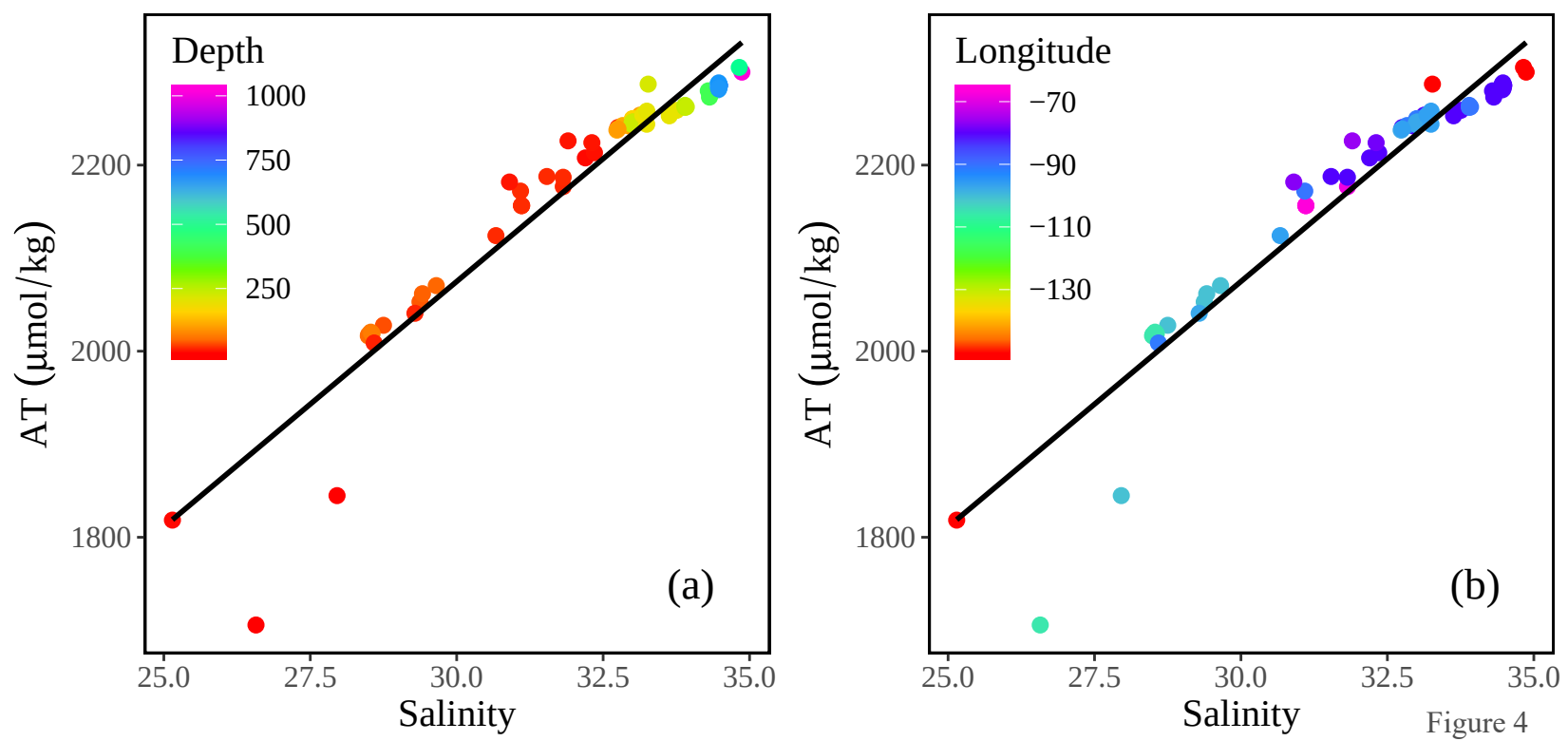
Depth
1000
750
500
250
AT (µmol/kg)
2200
2000
1800
25.0
27.5
30.0
32.5
35.0
Salinity
(a)
Longitude
−70
−90
−110
−130
AT (µmol/kg)
2200
2000
1800
25.0
27.5
30.0
32.5
35.0
Salinity
(b)

Figure 4

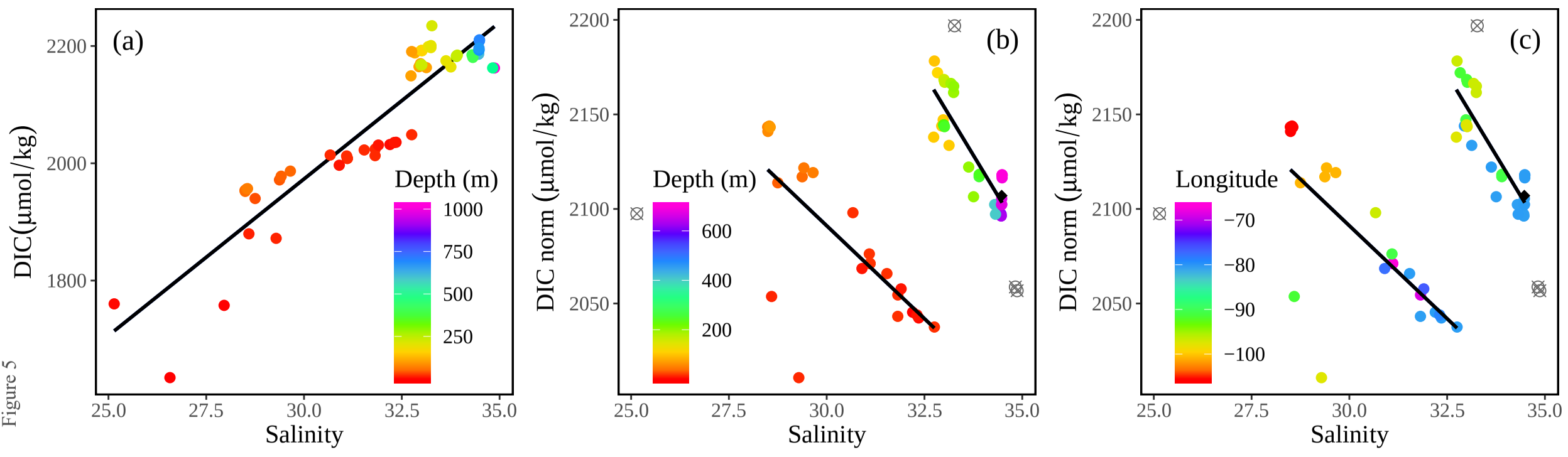
(a)
DIC(µmol/kg)
2200
2000
1800
Depth (m)
1000
750
500
250
25.0
27.5
30.0
32.5
35.0
Salinity
(b)
DIC norm (µmol/kg)
2200
2150
2100
2050
Depth (m)
600
400
200
Salinity
(c)
DIC norm (µmol/kg)
Longitude
−70
−80
−90
−100
Salinity

Figure 5

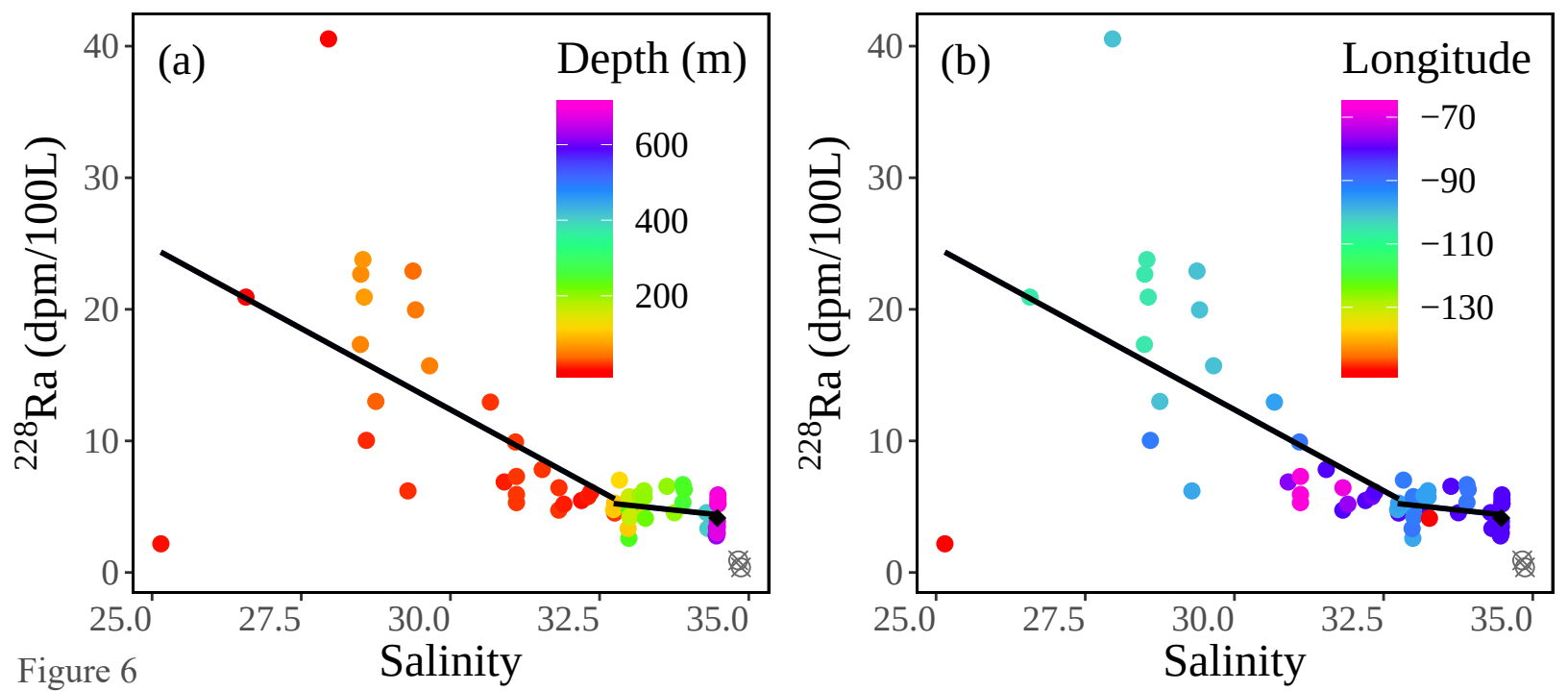
(a)
Depth (m)
600
400
200
(b)
Longitude
−70
−90
−110
−130
$^{228}$Ra (dpm/100L)
Salinity
0
10
20
30
40
25.0
27.5
30.0
32.5
35.0

Figure 6

Figure 7

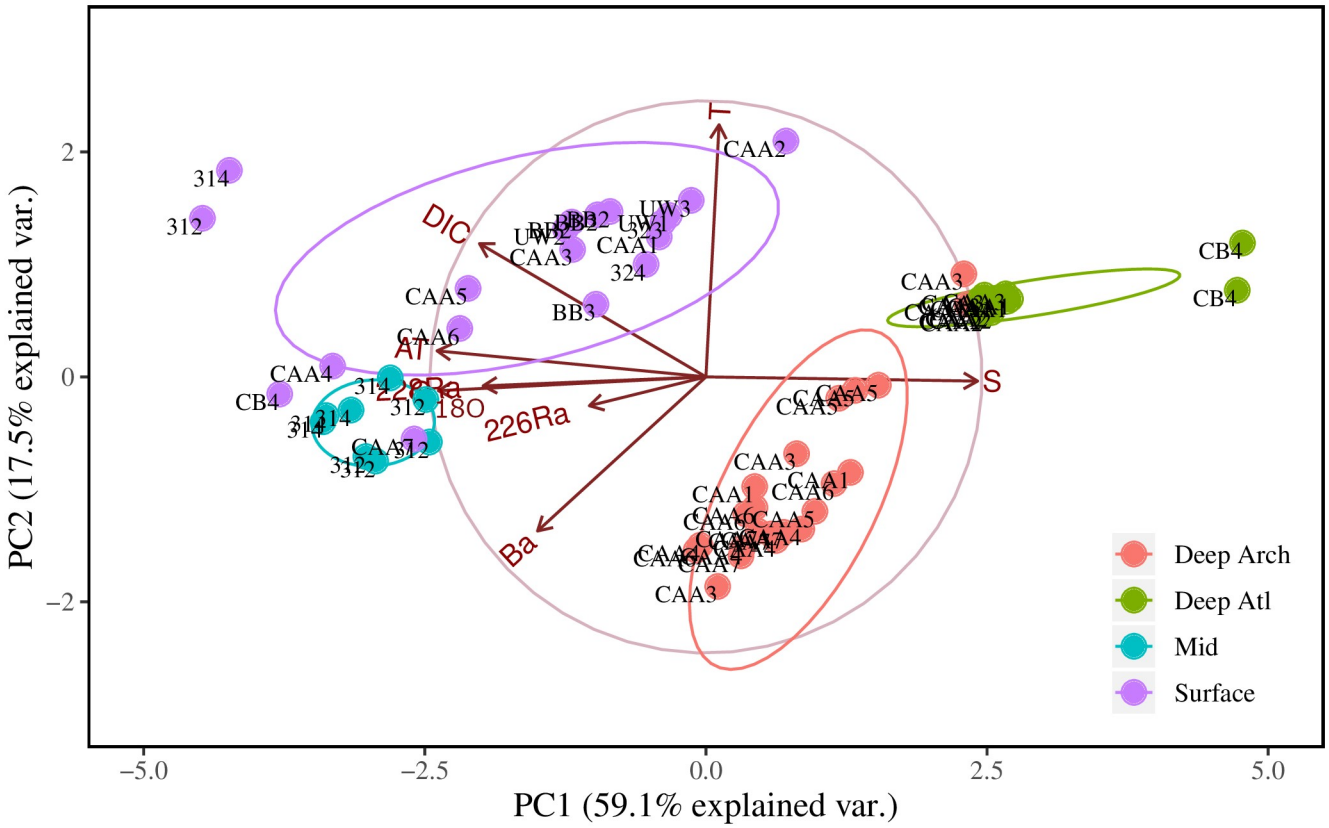
PC2 (17.5% explained var.)
PC1 (59.1% explained var.)
2
0
−2
−5.0
−2.5
0.0
2.5
5.0
T
S
DIC
AT
Ba
226Ra
228Ra
18O
Deep Arch
Deep Atl
Mid
Surface

Figure 8

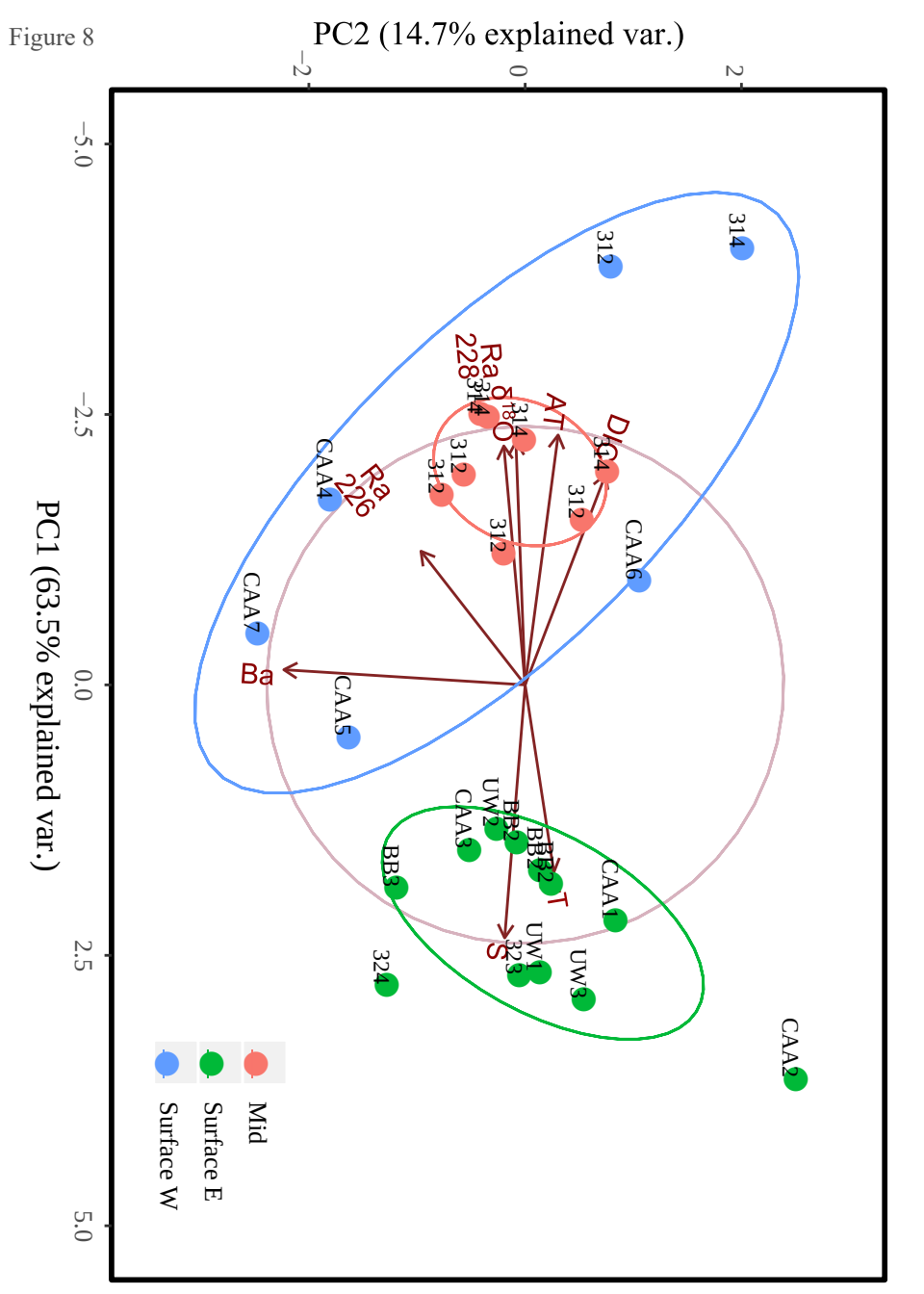
PC2 (14.7% explained var.)
PC1 (63.5% explained var.)
−2
0
2
−5.0
−2.5
0.0
2.5
5.0
314
312
CAA6
CAA4
CAA7
CAA5
CAA3
CAA1
CAA2
BB3
BB2
UW1
UW2
UW3
324
323
Ra 228
δ18O
AT
Dp
Ra 226
Ba
T
S
Mid
Surface E
Surface W

Figure 9

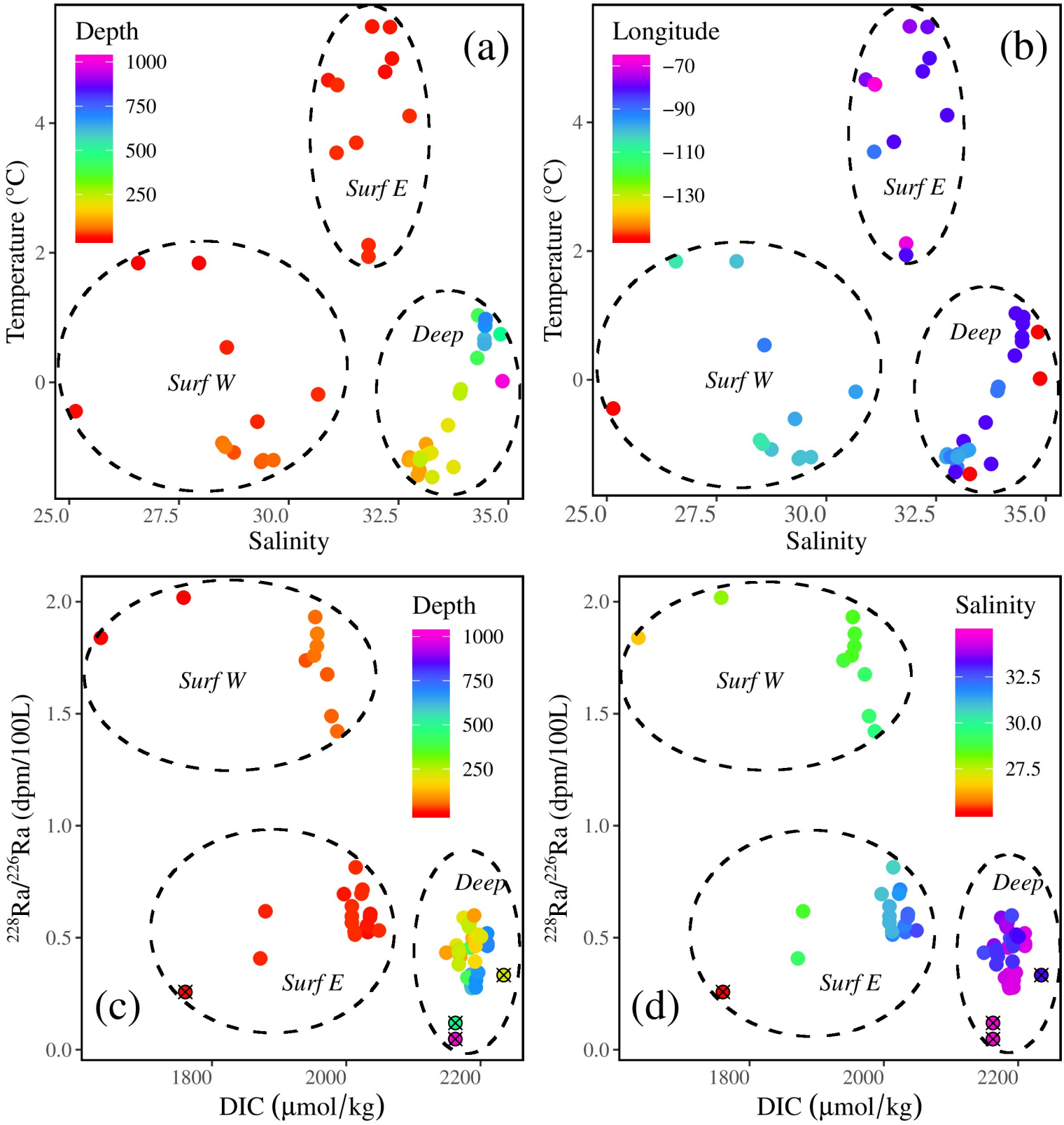
Depth
1000
750
500
250
(a)
Surf E
Surf W
Deep
Temperature (°C)
Salinity
Longitude
−70
−90
−110
−130
(b)
(c)
(d)
$^{228}Ra/^{226}Ra$ (dpm/100L)
DIC (μmol/kg)
Salinity
32.5
30.0
27.5

Figure 10

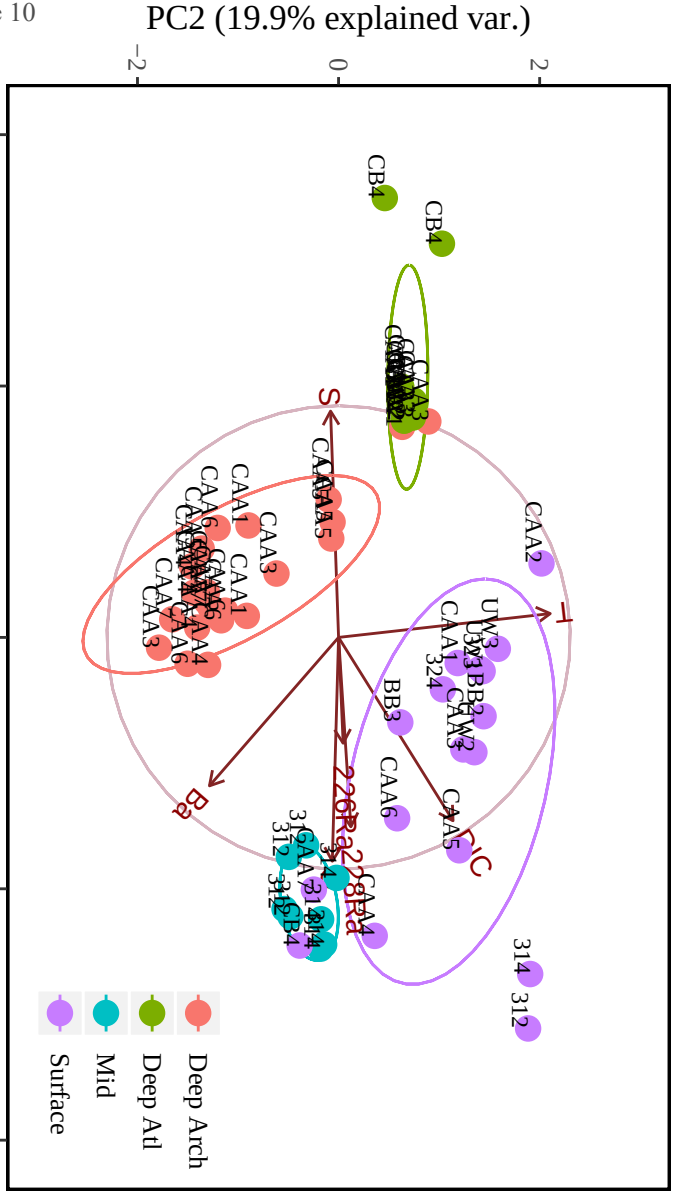
PC2 (19.9% explained var.)
PC1 (54.4% explained var.)
Deep Arch
Deep Atl
Mid
Surface

Figure 11

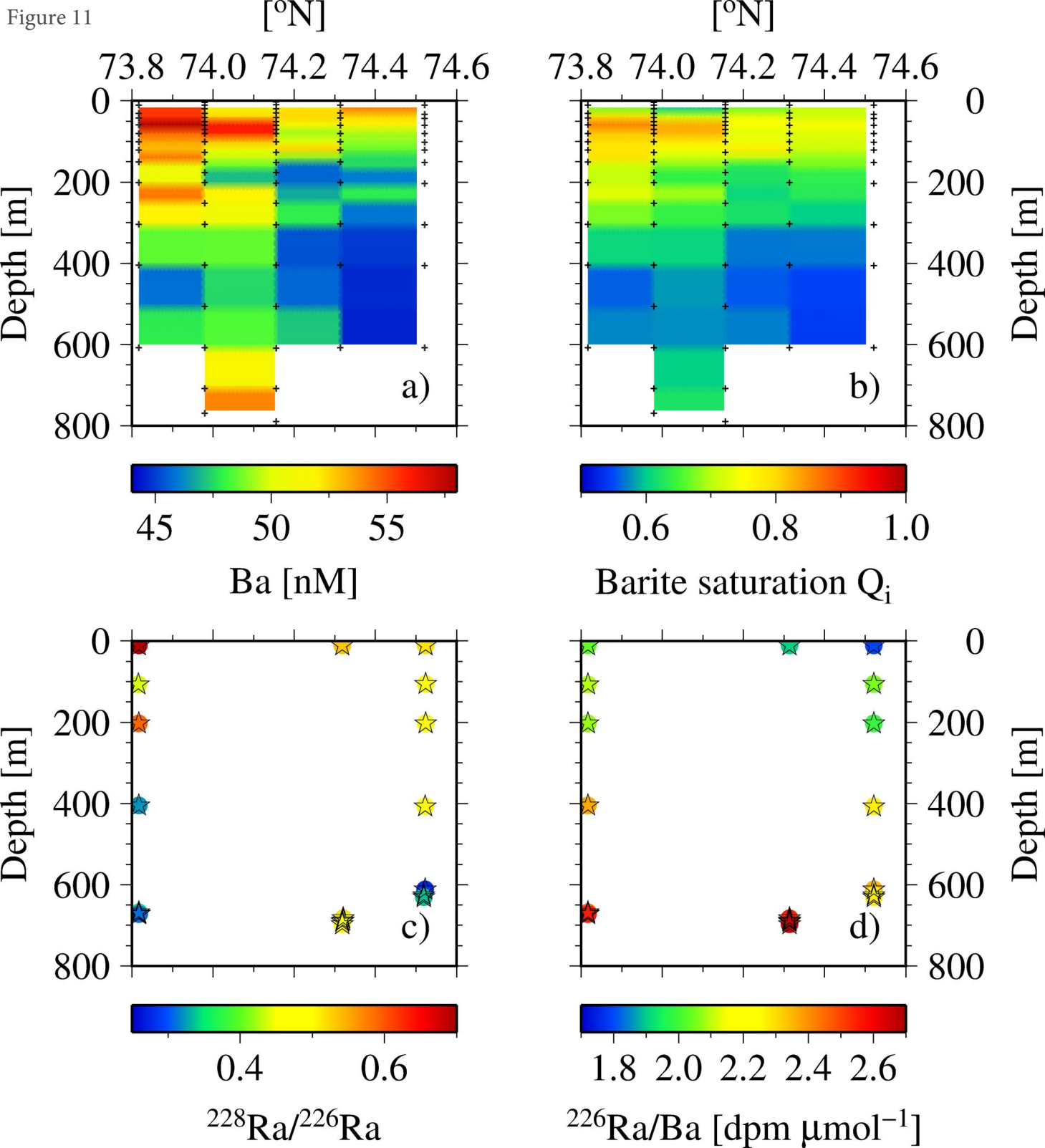
[°N]
73.8 74.0 74.2 74.4 74.6
Depth [m]
0
200
400
600
800
a)
45 50 55
Ba [nM]
b)
0.6 0.8 1.0
Barite saturation $Q_i$
c)
0.4 0.6
$^{228}Ra/^{226}Ra$
d)
1.8 2.0 2.2 2.4 2.6
$^{226}Ra/Ba$ [dpm µmol$^{-1}$]

Figure 12

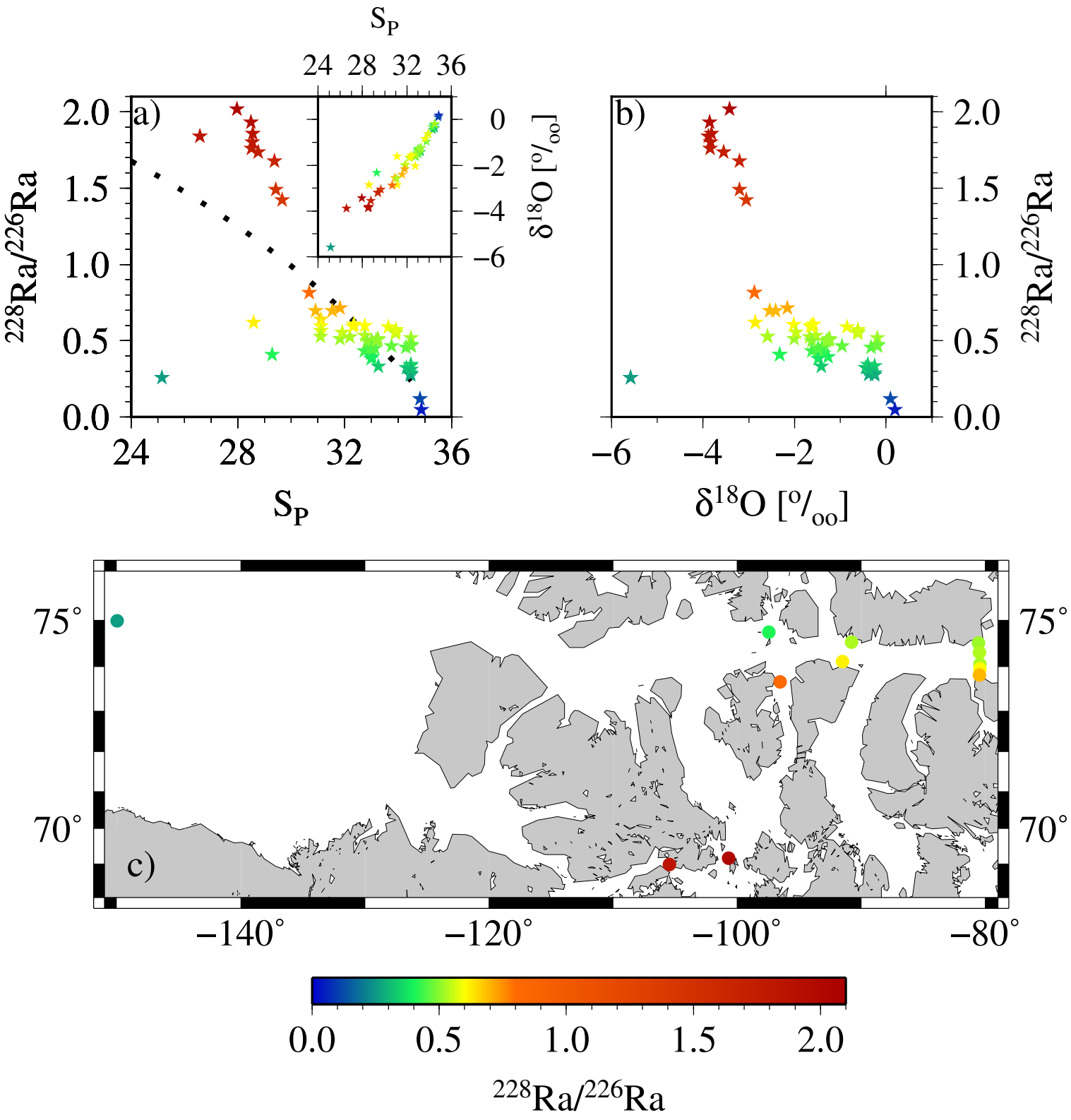
a)
b)
c)
$S_P$
$\delta^{18}O$ [‰]
$^{228}Ra/^{226}Ra$
2.0
1.5
1.0
0.5
0.0
24
28
32
36
0
−2
−4
−6
75°
70°
−140°
−120°
−100°
−80°

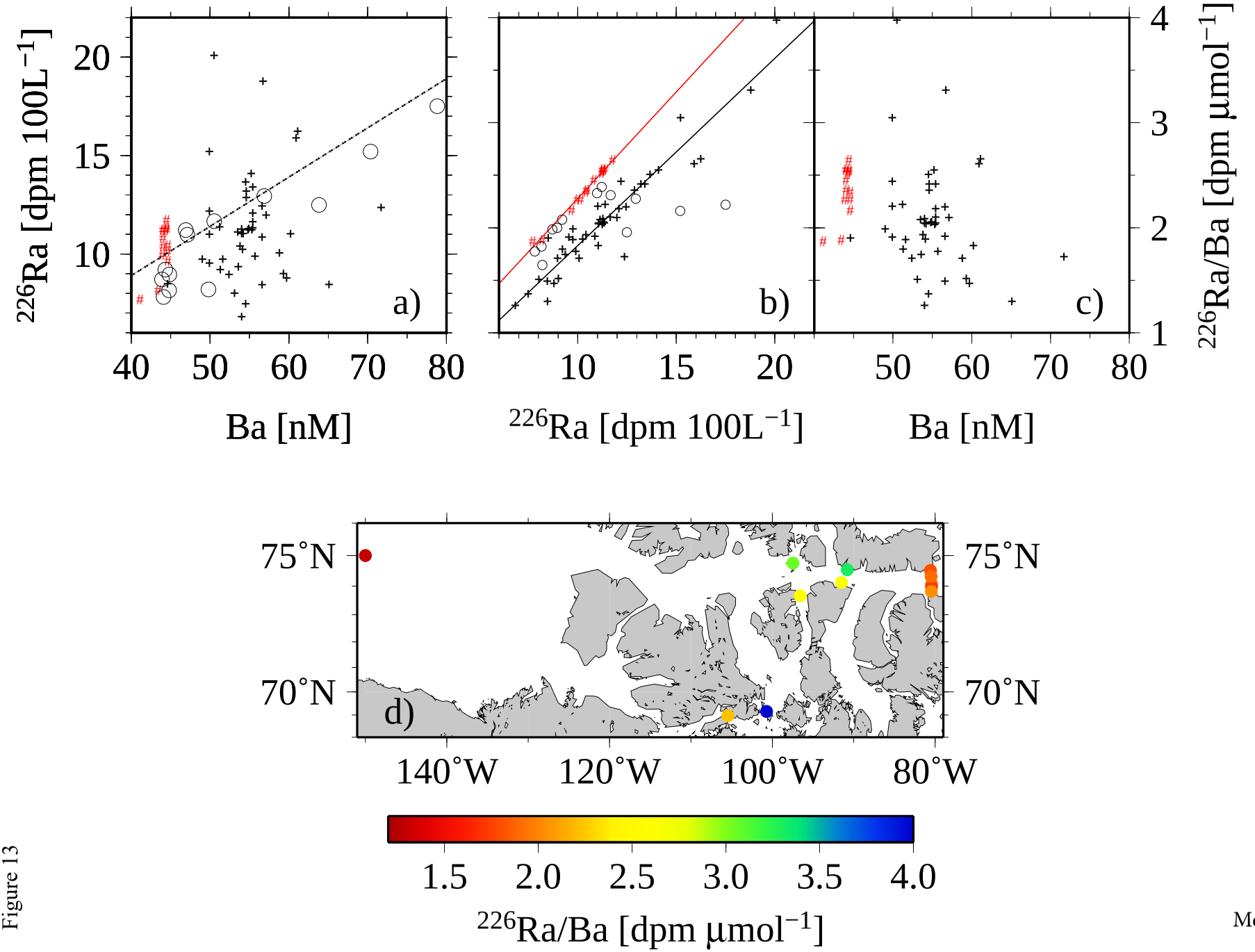


Figure 13

Mears et al., Figure 13

Figure 14

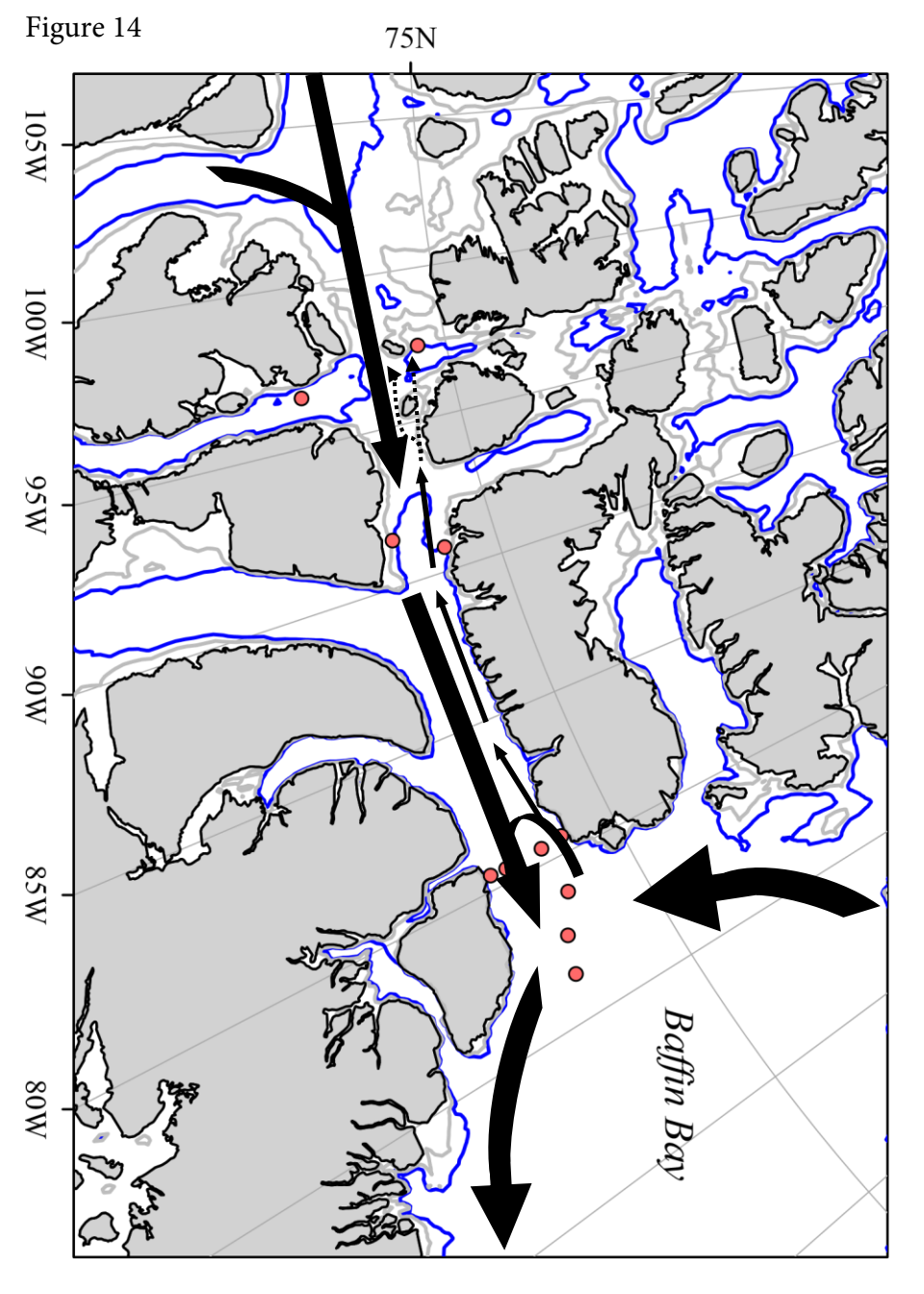

| Parameter | Equation to Normalize |
|---|---|
| T | $T_0 = \arccos(((5.5\text{-}T)/\max(5.5\text{-}T))^2)$ |
| S | $S_0 = \arcsin((S/\max(S))^{1/2})$ |
| DIC | $DIC_0 = (\max(DIC) - DIC)^{1/3}$ |
| $\delta^{18}O$ | $\delta^{18}O_0 = ((\max(\delta^{18}O) +1) - \delta^{18}O)^{1/2}$ |
| $^{226}Ra$ | $^{226}Ra_0 = {}^{226}Ra^{1/3}$ |
| $^{228}Ra$ | $^{228}Ra_0 = \log_{10}({}^{228}Ra)$ |
| Ba | $Ba_0 = Ba^{1/2}$ |

DIC (µmol/kg) | AT (µmol/kg) | $\delta O^{18}$ | Ba (nM)

Depth(m): 100, 300, 500, 700

PML
PML–UHL
UHL–ATL

CAA1 | CAA2 | CAA3 | CAA4 | CAA5 | CAA6 | CAA7 | CB4 | 312 | 314

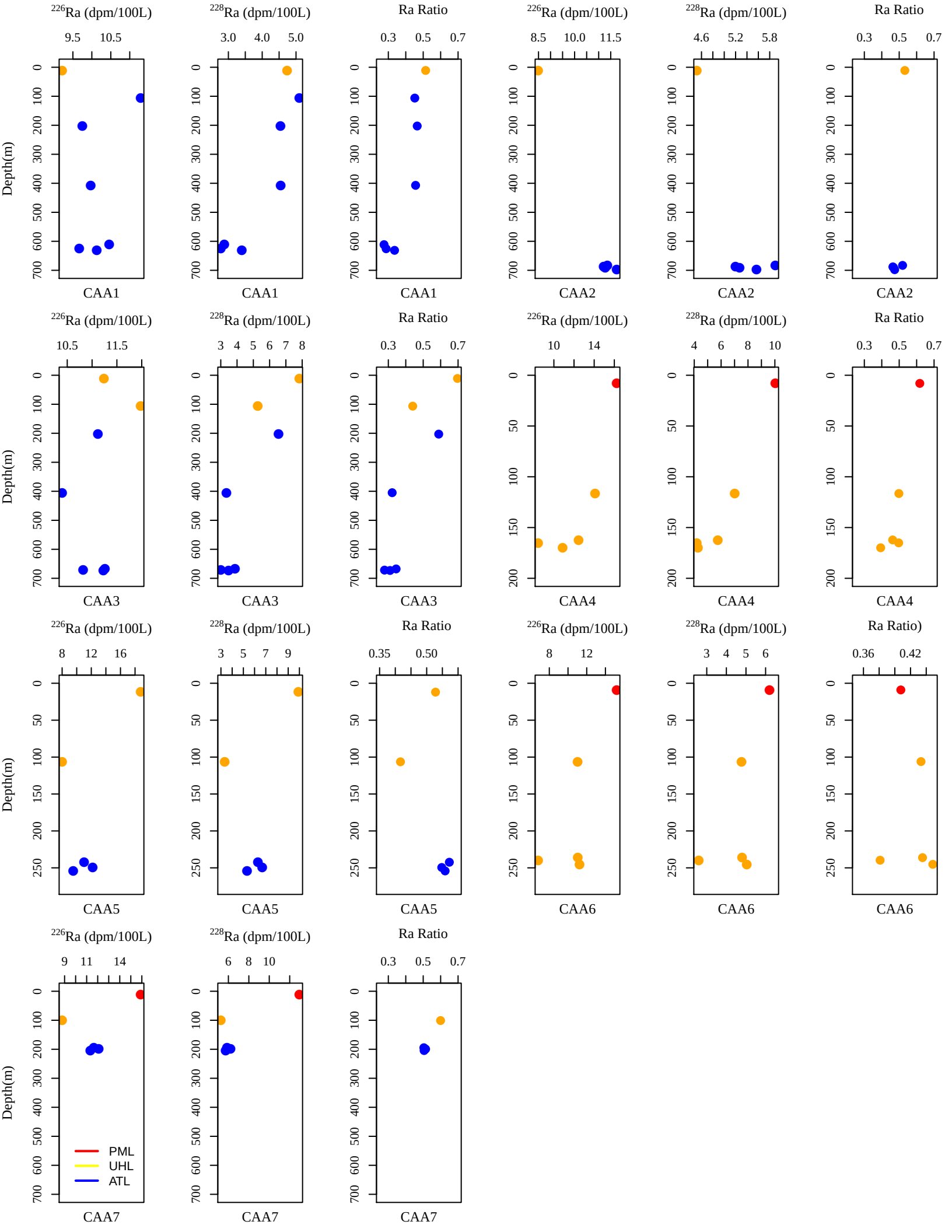
226Ra (dpm/100L)
228Ra (dpm/100L)
Ra Ratio
Depth(m)
CAA1
CAA2
CAA3
CAA4
CAA5
CAA6
CAA7
PML
UHL
ATL